The Astronomical Journal, 146:160 (18pp), 2013 December doi:10.1088/0004-6256/146/6/160

DEPLETED GALAXY CORES AND DYNAMICAL BLACK HOLE MASSES

S. P. Rusli[1,2], P. Erwin[1,2], R. P. Saglia[1,2], J. Thomas[1,2], M. Fabricius[1,2], R. Bender[1,2], and N. Nowak[3]
[1] Max-Planck-Institut für extraterrestrische Physik, Giessenbachstrasse, D-85748 Garching, Germany
[2] Universitäts-Sternwarte München, Scheinerstrasse 1, D-81679 München, Germany
[3] Max-Planck-Institut für Physik, Föhringer Ring 6, D-80805 München, Germany
Received 2012 July 27; accepted 2013 October 15; published 2013 November 11

ABSTRACT

Shallow cores in bright, massive galaxies are commonly thought to be the result of scouring of stars by mergers of binary supermassive black holes. Past investigations have suggested correlations between the central black hole mass and the stellar light or mass deficit in the core, using proxy measurements of $M_{\rm BH}$ or stellar mass-to-light ratios (Υ). Drawing on a wealth of dynamical models which provide both $M_{\rm BH}$ and Υ, we identify cores in 23 galaxies, of which 20 have direct, reliable measurements of $M_{\rm BH}$ and dynamical stellar mass-to-light ratios ($\Upsilon_{\star,\rm dyn}$). These cores are identified and measured using Core-Sérsic model fits to surface brightness profiles which extend out to large radii (typically more than the effective radius of the galaxy); for approximately one-fourth of the galaxies, the best fit includes an outer (Sérsic) envelope component. We find that the core radius is most strongly correlated with the black hole mass and that it correlates better with total galaxy luminosity than it does with velocity dispersion. The strong core-size–$M_{\rm BH}$ correlation enables estimation of black hole masses (in core galaxies) with an accuracy comparable to the $M_{\rm BH}$–σ relation (rms scatter of 0.30 dex in log $M_{\rm BH}$), without the need for spectroscopy. The light and mass deficits correlate more strongly with galaxy velocity dispersion than they do with black hole mass. Stellar mass deficits span a range of 0.2–39 $M_{\rm BH}$, with almost all (87%) being $<10\,M_{\rm BH}$; the median value is 2.2 $M_{\rm BH}$.

Key words: galaxies: elliptical and lenticular, cD – galaxies: kinematics and dynamics – galaxies: nuclei – galaxies: photometry

Online-only material: color figures, extended figure

1. INTRODUCTION

In the present-day view, mergers are a common and important way of building up massive elliptical galaxies. With the presence of supermassive black holes in the centers of most galaxies (Kormendy & Richstone 1995; Magorrian et al. 1998; Richstone et al. 1998), merger processes are thought to have left signatures on the central structure of the remnant galaxies. Begelman et al. (1980) suggest that a binary black hole that is formed by the merger of two galaxies scours the stars from the center of the newly created system as the binary shrinks. The energy liberated by the hardening of the binary evacuates the central part through the ejection of surrounding stars, causing less light in the center.

Hubble Space Telescope (*HST*) observations of galaxy nuclei see two kinds of behavior in the central light profiles of ellipticals, traditionally classified as "power-law" and "core" galaxies (Kormendy et al. 1994; Ferrarese et al. 1994; Lauer et al. 1995, 2005; Byun et al. 1996; Lauer et al. 2007). The power-law profiles took their name from their approximation by a single power law at small radii ($r \lesssim 10$ or $20''$). More modern interpretations have emphasized that these profiles can be better understood as the inward continuation of the galaxy's overall Sérsic profile, usually modified by an additional, nuclear-scale stellar component (Graham et al. 2003; Trujillo et al. 2004; Ferrarese et al. 2006; Kormendy et al. 2009). The core galaxy, in contrast, displays a surface brightness profile with a distinct break from a steep outer slope to a shallower inner cusp. Core profiles mainly occur in very luminous elliptical galaxies and are considered the result of dissipationless mergers of two galaxies that have central black holes.

Much numerical work has been done to explore the binary black hole idea. The work of Ebisuzaki et al. (1991) suggests that the stellar mass ejected from the core is comparable to the mass of the central black hole $M_{\rm BH}$. Makino & Ebisuzaki (1996) find that core radius roughly doubles after each major merger. Nakano & Makino (1999), using isothermal King models, suggest that the core size should scale with the final $M_{\rm BH}$. Simulations performed by Milosavljević & Merritt (2001) show for the first time that merging two galaxies with steep cusps can result in a merger remnant with a shallow power-law cusp in the inner part (core). Merritt (2006) is the first to quantify the magnitude of the mass deficit (or the mass ejected by the binary) with respect to the galaxy's merger history. By following the binary evolution up to the stalling radius, he formulates the mass deficit to be $0.5\,NM_{\rm BH}$ with N as the number of major merger events. An investigation into the post-coalescence stage of the binary suggests that the mass deficit could still be larger. This is because the coalescing binary emits gravitational waves which impart a kick on the merged black hole and eject it from the center. Due to dynamical friction, the resulting oscillations of the black hole would gradually damp, returning it to the center of the galaxy and ejecting more stars from the core. This process could increase the mass deficit existing before the binary coalescence by up to $5M_{\rm BH}$ for a single merger (Gualandris & Merritt 2008).

Several publications in the past have performed function fitting to galaxy profiles in order to quantify the core parameters such as the core size, the deficit in light or mass, and to analyze the correlation between these core properties and $M_{\rm BH}$ or the global properties of the galaxies (Graham 2004; Ferrarese et al. 2006; Lauer et al. 2007, Kormendy et al. 2009, hereafter KFCB09; Kormendy & Bender 2009, hereafter KB09; Richings et al. 2011; Dullo & Graham 2012, 2013; see also Kormendy & Ho 2013). These studies are based on different samples, data sets, approaches, parameterizations, and assumptions, which apparently lead to different, partly systematic, core quantities.

The most important difference is the amount of central mass deficit with respect to the black hole mass that can be expected in core galaxies. Graham (2004) and Ferrarese et al. (2006) find an average mass deficit of around twice the black hole mass, Dullo & Graham (2012) derive central mass deficits of about 0.5–4 $M_{\rm BH}$, while KFCB09 find their mean mass deficit to be 10.5 $M_{\rm BH}$. Aside from that, each of these studies has a drawback in at least one of three aspects crucial to achieving high accuracy.

The first is the radial range of the surface brightness profiles. Lauer et al. (2007), Richings et al. (2011), and Dullo & Graham (2012) fit galaxy profiles that extend typically to only 10–20″. Moreover, it appears that some galaxy profiles in Dullo & Graham (2012), which are taken from Lauer et al. (2005, hereafter L05), suffer from oversubtraction of the sky that biases the core-Sérsic fits (see Section 5). A full galaxy profile is necessary to properly measure the outer profile, to optimally remove the sky background, and thus to provide better constraints on the light and mass deficit.

The second is the determination of the stellar mass-to-light ratio ($\Upsilon_\star$) to convert the light deficit to the mass deficit. In the past studies, either different values are assigned to the galaxies according to their luminosities (Ferrarese et al. 2006; KFCB09) or a constant value is assumed for all the galaxies in the sample (Graham 2004; Dullo & Graham 2012). This of course introduces additional uncertainties and biases in deriving the mass deficits.

The last important aspect lies in the black hole masses, which are mostly derived from outdated black hole–bulge relations, especially the ones between $M_{\rm BH}$ and the velocity dispersion of the host bulge ($M_{\rm BH}$–σ relation). The majority of core galaxies are bright massive elliptical galaxies. For this class of galaxies Lauer et al. (2007) find that the $M_{\rm BH}$–L relation predicts a higher density of massive black holes ($\sim 10^{10}\ M_\odot$) compared to the $M_{\rm BH}$–σ relation. Furthermore, the $M_{\rm BH}$–σ relation used in these papers also fails to predict the existence of the largest black holes ($M_{\rm BH} > 10^{10} M_\odot$) that are found in distant quasars (Shields et al. 2006) in the sample of local galaxies. The recent finding of black holes of 10 billion solar masses (McConnell et al. 2011a; van den Bosch et al. 2012), which might be the missing link between the local black holes and the massive distant quasars, further supports the indications that the previous $M_{\rm BH}$–σ relations for massive bright early type galaxies need to be reevaluated (e.g., Kormendy & Ho 2013). In addition, most previous studies have used $M_{\rm BH}$ measurements (or $M_{\rm BH}$–σ relations based on $M_{\rm BH}$ measurements) which did not include dark-matter halos in the modeling. $M_{\rm BH}$ values typically increase by ∼20% (Schulze & Gebhardt 2011) or 30% (Rusli et al. 2013, hereafter Paper I) when dark matter is included in the modeling, but the increase can be as large as a factor of six when the black hole's sphere of influence is not well resolved (McConnell et al. 2011b). In the particular sample that we use in this paper, which includes brightest cluster galaxies (BCGs), we find that the measured black hole mass is on average more than 3 times higher than that predicted by the $M_{\rm BH}$–σ relation (e.g., Tremaine et al. 2002; Gültekin et al. 2009; Graham et al. 2011).

In this paper, we combine improved core-property measurements with new measurements and present the analysis of possible relations between the core and black hole mass or the galaxy properties. We use only directly measured black hole masses and consequently avoiding scatter and possible biases inherent in using proxy measurements. We use dynamically-determined, individual stellar mass-to-light ratios ($\Upsilon_{\star,\rm dyn}$) to estimate the mass deficit, instead of relying on a scaling function or a constant value. We also use full galaxy profiles in the fitting and the quantification of the core parameters. Our analysis is based on a sample of 20 galaxies; seven of these galaxies are taken from Paper I, in which the black hole masses and $\Upsilon_{\star,\rm dyn}$ are derived taking into account the presence of dark matter halos. For completeness, we add a further 3 galaxies to the sample; they are not included in the main sample due to the lack of reliable literature sources for the black hole masses. In order to derive the mass deficit, we assume that the original (pre-scouring) profile is the extrapolated Sérsic profile that fits the light distribution at large radii. In Section 2, we describe the method that we use to identify the core galaxies and to fit the observed surface brightness profiles. In Section 3, we present the best-fitting models for each galaxy; cases where galaxies are best fit with the addition of an outer envelope are discussed in Section 4. We compare the fitting results with previous studies in Section 5. Section 6 presents the details of how the luminosity and mass deficit in the core are computed based on the best-fitting models. The core-related quantities derived in Sections 3 and 6 are compared with the black hole mass, velocity dispersion, and galaxy luminosity in Section 7. The last section discusses and summarizes the results.

2. THE METHOD

2.1. Identifying Cores

All of the photometric profiles examined in this work are quite extended, reaching out to at least 9 kpc. Therefore, we base our analysis on a function that is designed to fit not just the inner or the outer part of galaxies, but rather the galaxy as a whole. To identify core galaxies, we follow the criteria in Graham et al. (2003) and Trujillo et al. (2004), who define the core as "a downward deviation from the inward extrapolation of the outer (Sérsic) profile." This involves fitting the galaxy in question with both the Sérsic and the core-Sérsic functions.

The Sérsic profile (Sérsic 1963, 1968) is written as:

$$I(r) = I_e \exp\left\{-b_n\left[\left(\frac{r}{r_e}\right)^{1/n} - 1\right]\right\}. \quad (1)$$

I_e is the intensity at r_e, the projected half-light radius. n is called the Sérsic index which describes the shape or curvature of the light profile. The quantity b_n is a function of n, defined in such a way that r_e encloses half of the total luminosity. We approximate $b_n \sim 2n - 1/3 + 4/405n + \ldots$ by using the asymptotic expansion of Ciotti & Bertin (1999), Equation (18) for $n > 0.36$. Many other approximation formulas are available and are summarized in Graham & Driver (2005). For $n = 1$, the Sérsic function reduces to an exponential function and for $n = 4$, it becomes the de Vaucouleurs profile (de Vaucouleurs 1948).

The core-Sérsic function introduced by Graham et al. (2003) and Trujillo et al. (2004) is expressed as:

$$I(r) = I'\left[1 + \left(\frac{r_b}{r}\right)^{\alpha}\right]^{\gamma/\alpha} \exp\left[-b_n\left(\frac{r^\alpha + r_b^\alpha}{r_e^\alpha}\right)^{1/n\alpha}\right] \quad (2)$$

with

$$I' = I_b 2^{-\gamma/\alpha} \exp[b_n(2^{1/\alpha} r_b/r_e)^{1/n}]. \quad (3)$$

This profile consists of a Sérsic profile in the outer part, specified by the projected half-light radius r_e and the Sérsic index n, and a power-law profile in the inner part with a slope of γ. The change from one to another regime occurs at the break radius

r_b and the sharpness of the transition is specified by the parameter α. Higher values of α mean sharper transitions. b_n is approximated in the same way as for the Sérsic function.

We summarize four criteria in Trujillo et al. (2004) that we use to identify core galaxies below. In Section 3 we examine each criterion.

1. A characteristic pattern should be visible in the residuals when fitting a Sérsic profile to an idealized core galaxy. This serves as a qualitative evidence.
2. A core-Sérsic function gives a significantly better fit than a Sérsic model. Quantitatively, it is expected that the reduced χ^2 value for the Sérsic fit χ^2_S is larger than twice that of the core-Sérsic fit χ^2_{CS}.
3. To avoid an ambiguous core detection, the potential core must be well-resolved by the data. Quantitatively, r_b should be $>r_2$ where r_2 is the second innermost data point in the observed profile.
4. The power-law slope has to be consistently less than the slope of the Sérsic fit inside r_b.

We decided to adopt an additional criterion based on resolution limits. Trujillo et al. did not include such a limit, partly because many of their profiles did not probe radii smaller than the *HST* resolution limit due to dust, etc.; however, they did note that one of their "possible core" galaxies (NGC 3613) had a break radius smaller than the resolution limit of 0.″16 originally suggested by Faber et al. (1997). The latter limit is ∼2 times the FWHM of most of the PC data used by Faber et al. (1997); generalizing this, we suggest the following additional criterion.

5. The potential core should have $r_b \gtrsim 2$ the FWHM of the imaging data used for the innermost part of the profile. For most of the galaxies considered in this paper, which use optical WFPC2 or ACS/WFC data, this corresponds to $r_b \gtrsim$ 0.″15; for two galaxies using NICMOS2 data (NGC 4261 and NGC 4374), the limit would be ≈0.″26, and for NGC 1550, where we use SINFONI data with an FWHM of 0.″17, the limit would be 0.″34.

2.2. The Fitting Procedure

We construct a one-dimensional light profile along the circularized radius (mean profile), instead of along the semimajor radius as is commonly done. The circularized radius is defined as $r = \sqrt{ab}$ where a and b are the semimajor and semiminor axes radius of the isophote. This way, we take into account the variation of ellipticity with radius, giving a fair representation of the isophotes. The use of this mean profile is consistent with the implementation of the point-spread function (PSF) correction (Section 2.3).

The fitting is done using a one-dimensional profile fitting software written by P. Erwin. An initial model is generated based on user-given starting values. It is compared to the observed profile and the χ^2 is calculated. The best-fitting solution is achieved by minimizing the χ^2 of the fit, using the Levenberg–Marquardt algorithm (Levenberg 1944; Marquardt 1963). The user provides a starting value and its range of allowed values for each free parameter of the model. There are three free parameters in the Sérsic model, i.e., n, r_e, I_e, and there are six free parameters in the core-Sérsic model, i.e., n, r_b, r_e, μ_b, α, γ.

Since we are mainly interested in the inner region of the galaxy, the blurring of the central light profile by the PSF becomes important and has to be taken into account. For several galaxies, the photometric profiles are derived from deconvolved images (see Table 1). We fit these profiles as described in the previous paragraph. For the other galaxies we incorporate a PSF correction routine, described in the next section, into the fitting program such that the initial model is convolved first before being compared to the observed light profile. In this case, the minimized χ^2 represents the difference between the convolved model and the data. The PSF convolution is done at every iteration.

2.3. The Implementation of the PSF Convolution

For galaxies whose light profiles are not seeing-corrected, we take the PSF into account in the fitting by means of convolution. We use the PSF corresponding to the galaxy image used to derive the innermost galaxy isophotes. For the galaxies from Paper I, the PSF image is the same one that was used in the deprojection. For the other galaxies, the PSF image is generated using TinyTim by supplying the appropriate filter and camera. From the image, we generate a circularized profile of the PSF by averaging its radial profile at different azimuthal angles (done using MIDAS). We further normalize the PSF profile such that the total flux is one. The implementation of the convolution follows Saglia et al. (1993, their Appendix A). Below, we review the method.

The PSF convolution is carried out by multiplying the galaxy surface brightness profile and the PSF in the Fourier space. On the sky, the galaxy surface brightness is a function of a two-dimensional position $\mathbf{r}$ and so is the PSF. If $I(\mathbf{r})$ and $P(\mathbf{r})$ denote the surface brightness and the PSF distribution, then the convolved surface brightness profile becomes

$$I_{\rm conv}(\mathbf{r}) = \int \exp(i\mathbf{k}\cdot\mathbf{r})\,\hat{P}(\mathbf{k})\,\hat{I}(\mathbf{k})\frac{d^2k}{(2\pi)^2}, \tag{4}$$

where

$$\hat{I}(\mathbf{k}) = \int \exp(i\mathbf{k}\cdot\mathbf{r})\,I(\mathbf{r})\,d^2r$$
$$\hat{P}(\mathbf{k}) = \int \exp(i\mathbf{k}\cdot\mathbf{r})\,P(\mathbf{r})\,d^2r. \tag{5}$$

Since we use a one-dimensional, circularized surface brightness profile, I or P are a function of only the radius r. In this case, $\int_0^{2\pi} \exp(ikr\cos\theta)\,d\theta = 2\pi J_0(kr)$, where $J_0(kr)$ is the Bessel function of the order of zero. Then, Equation (4) becomes

$$I_{\rm conv}(r) = \int_0^\infty \frac{1}{2\pi} J_0(kr)\,\hat{P}(k)\,\hat{I}(k)\,k\,dk, \tag{6}$$

with

$$\hat{P}(k) = \int_0^\infty 2\pi\,P(r)J_0(kr)r\,dr \tag{7}$$

$$\hat{I}(k) = \int_0^\infty 2\pi\,I(r)J_0(kr)r\,dr. \tag{8}$$

In this way, although the surface brightness and PSF profiles are one-dimensional, the convolution is implemented such that the light coming from different angles is also taken into account. This is important because the light is scattered, due to the seeing, not only in the radial but also in the azimuthal direction. Equations (6)–(8) are also called the Hankel transform. We compute the convolved surface brightness profile numerically, making use of integration routines in the GNU Scientific Library.

Figure 1 shows how well this convolution works in the case of circular (upper profiles) and non-circular (lower profiles) images. For the former, we generate a galaxy image which follows

Table 1
Galaxies Suspected to Have Depleted Cores

Galaxy	Type	Distance (Mpc)	Filter	σ_e (km s^{-1})	M_V (mag)	$M_{\rm BH}$ ($M_\odot$)	$\Upsilon_{\star,\rm dyn}$
IC 1459	E3	30.9 [5]	V [1]	315.0 [5]	−22.57 [5]	$2.8(1.6, 3.9) \times 10^9$ [19]	4.5(4.1, 5.0) † [20]
NGC 1374	E	19.23 [2]	B, R [2,8]	166.8 [2]	−20.37 [2]	$5.8(5.3, 6.3) \times 10^8$ [2]	5.3(4.7, 5.9) [2]
NGC 1399	E1	21.1 [5]	B [1]	296.0 [5]	−22.12 [5]	$9.1(4.4, 18) \times 10^8$ [21,22]	10.2(9.7, 10.5) † [23]
NGC 1407	E0	28.05 [2]	B* [2]	276.1 [2]	−22.73 [2]	$4.5(4.1, 5.4) \times 10^9$ [2]	6.6(5.8, 7.5) [2]
NGC 1550	E2	51.57 [2]	R [2]	270.1 [2]	−22.30 [2]	$3.7(3.3, 4.1) \times 10^9$ [2]	4.0(3.4, 4.5) [2]
NGC 3091	E3	51.25 [2]	I [2]	297.2 [2	−22.66 [2]	$3.6(3.4, 3.7) \times 10^9$ [2]	3.8(3.6, 4.1) [2]
NGC 3379	E1	10.57 [4]	I* [1]	206.0 [5]	−20.99 [4]	$4.1(3.1, 5.1) \times 10^8$ [9]	2.8(2.6, 3.0) † [9]
NGC 3608	E2	23.0 [18]	V [1]	182.0 [5]	−21.05 [5]	$4.7(3.7, 5.7) \times 10^8$ [18]	3.1(2.8, 3.4) † [18]
NGC 3842	E	98.40 [6]	V* [1]	270.0 [5]	−23.17 [5]	$9.7(7.2, 12.7) \times 10^9$ [6]	6.7(5.6, 7.7) † [6]
NGC 4261	E2	31.60 [3]	V* [3]	315.0 [5]	−22.60 [4]	$5.2(4.1, 6.2) \times 10^8$ [13]	9.1(7.9, 10.3) †[15]
NGC 4291	E	25.0 [18]	V [1]	242.0 [5]	−20.67 [5]	$9.2(6.3, 1.21) \times 10^8$ [18]	5.4(4.7, 6.1) † [18]
NGC 4374	E1	18.45 [3]	V* [3]	296.0 [5]	−22.63 [4]	$9.2(8.4, 10.2) \times 10^8$ [14]	6.8(6.3, 7.2) [16]
NGC 4472	E2	17.14 [3]	V* [3]	300.2 [2]	−22.86 [2]	$2.5(2.4, 2.8) \times 10^9$ [2]	4.9(4.5, 5.3) [2]
NGC 4486	E0	17.22 [3]	V* [3]	324.0 [5]	−22.95 [4]	$6.2(5.7, 6.6) \times 10^9$ [10]	6.2(5.3, 6.9) † [10]
NGC 4552	E0	15.85 [3]	V* [3]	252.0 [24]	−21.37 [25]	$5.0(4.5, 5.5) \times 10^8$ ** [24]	7.1(6.7, 7.6) [16]
NGC 4649	E2	17.30 [3]	V* [3]	341.0 [5]	−22.75 [4]	$5.0(3.9, 6.1) \times 10^9$ [11]	7.3(6.5, 8.1) † [11]
NGC 4889	E4	103.2 [6]	R [12]	347.0 [5]	−23.72 [5]	$2.1(0.5, 3.7) \times 10^{10}$[6]	5.8(4.1, 7.4) † [6]
NGC 5328	E1	64.1 [2]	V [2]	332.9 [2]	−22.80 [2]	$4.7(2.8, 5.6) \times 10^9$ [2]	4.9(4.3, 5.5) [2]
NGC 5516	E3	58.44 [2]	R* [2]	328.2 [2]	−22.87 [2]	$3.3(3.0, 3.5) \times 10^9$ [2]	5.2(5.1, 5.5) [2]
NGC 5813	E1	32.2 [24]	i [1]	230.0 [24]	−22.06 [25]	$7.0(6.3, 7.7) \times 10^8$ ** [24]	4.7(4.4, 5.0) [16]
NGC 5846	E0	24.9 [24]	i [1]	238.0 [24]	−22.03 [25]	$1.1(1.0, 1.2) \times 10^9$ ** [24]	5.2(4.9, 5.5) [16]
NGC 6086	E	133.0 [17]	R* [1]	318.0 [17]	−23.12 [5]	$3.6(2.5, 5.3) \times 10^9$ [17]	4.2(3.6, 4.5) † [17]
NGC 7619	E	51.52 [2]	I [7]	292.2 [2]	−22.86 [2]	$2.5(2.2, 3.3) \times 10^9$ [2]	3.0(2.6, 3.3) [2]
NGC 7768	E	112.8 [6]	V [1]	257.0 [6]	−22.92 [6]	$1.3(0.9, 1.8) \times 10^9$ [6]	7.8(6.3, 9.3) † [6]

Notes. The number in square brackets refers to the literature source: [1] This paper (Appendices), [2] Paper I, [3] KFCB09, [4] KB09, [5] McConnell et al. (2011a), [6] McConnell et al. (2012), [7] Pu et al. (2010), [8] Lauer et al. (2005), [9] van den Bosch & de Zeeuw (2010), [10] Gebhardt & Thomas (2009), [11] Shen & Gebhardt (2010), [12] Thomas et al. (2007), [13] Ferrarese et al. (1996), [14] Walsh et al. (2010), [15] Häring & Rix (2004), [16] Cappellari et al. (2006), [17] McConnell et al. (2011b), [18] Schulze & Gebhardt (2011), [19] Cappellari et al. (2002), [20] Häring & Rix (2004), [21] Houghton et al. (2006), [22] Gebhardt et al. (2007), [23] Kronawitter et al. (2000), [24] Hu (2008) from Cappellari et al. (2008), [25] V_T^0 from de Vaucouleurs et al. (1991). For IC 1459, NGC 3379, NGC 4261, and NGC 4374 and the three objects with dubious black hole masses (see below), the $\Upsilon_{\star,\rm dyn}$ values come from single-component dynamical modeling (i.e., without dark matter; see the text). Whenever the literature source of $M_{\rm BH}$ or the mass-to-light ratio $\Upsilon_{\star,\rm dyn}$ is different from that for the distance, we write the values of $M_{\rm BH}$ or $\Upsilon_{\star,\rm dyn}$ after distance correction. Furthermore, we apply an extinction correction following Schlegel et al. (1998), as reported in NED, to the marked (†) $\Upsilon_{\star,\rm dyn}$ values, assuming they were not yet corrected. Column 4 is the photometric band of $\Upsilon_{\star,\rm dyn}$ and the light profile used in this paper; the asterisks in this column mark the galaxies whose innermost isophotes come from a deconvolved image, thus eliminating the need of PSF convolution during the fitting. The derivation of light profiles of NGC 3379, NGC 3842, NGC 6086, and NGC 7768 is described in the Appendices. For NGC 1399, we use the average $M_{\rm BH}$ from the two papers and take the extreme lower and upper limits of both measurements to define the error bar. For NGC 4552, NGC 5813, and NGC 5846, the quoted values are based on a single figure in a non-refereed publication. We do not consider these to be well-determined measurements, and mark them with asterisks; they are included in our plots but not used in our fits. We classify NGC 1550 and NGC 5516 as ellipticals, though literature classifications vary. Our extended kinematics and photometry show no signs of rotation or obvious (face-on) disks in these two galaxies.

a Sérsic law with $n = 4$ and zero ellipticity everywhere using the `makeimage` program from the two-dimensional image-fitting package IMFIT (P. Erwin, in preparation).[4] For the PSF, we create a circular Gaussian image with $\sigma = 1/40$ of the half-light radius of the galaxy model. We extract the radial profile of both images and use these to perform the one-dimensional convolution as described above. As an independent check, we separately convolve the galaxy image with the Gaussian image in IMFIT. The radial profile of this convolved image (I_{2D}) is compared to the result of the one-dimensional convolution (I_{1D}). The ratio is shown in the lower panel of the figure by the dashed line. This process is then repeated for a Sérsic image with an ellipticity of 0.4. The circularized profile of the convolved elliptical image is shown by the solid blue line and this is compared to the one-dimensional convolution result (the rectangles); the ratio of both is displayed as the solid line in the lower panel. The method works well in the case of a circular galaxy and shows a deviation of less than 0.02 mag arcsec^{-2} for an elliptical image; we have repeated this exercise for different Sérsic indices, resulting in similar conclusions. Since the ellipticity of 0.4 is larger than the ones measured in the majority of galaxies in our sample, we expect smaller errors in the actual galaxy case.

[4] http://www.mpe.mpg.de/~erwin/code/imfit

3. CORE-SÉRSIC VERSUS SÉRSIC FIT

The list of galaxies examined in this section is given in Table 1, along with the data sources. We compiled this list taking into account all galaxies which had both dynamically measured central black hole mass and evidence for cores, but in the end retained only those with clear evidence for a core *and* good enough data for measuring the core properties. The recent compilation of McConnell & Ma (2013) lists 9 more galaxies which we do not include: A1836-BCG, A3565-BCG (IC 4296), NGC 524, NGC 3607, NGC 4473, NGC 5077, NGC 5128, NGC 5576, and NGC 7052. Strong nuclear dust in

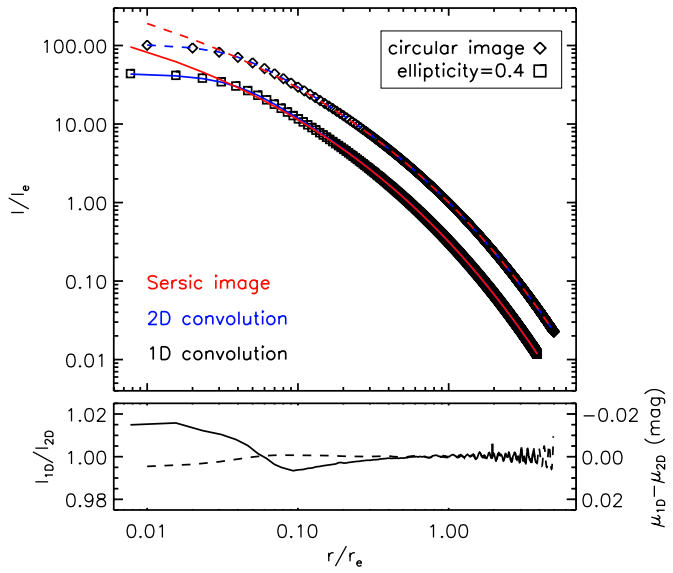

Figure 1. Top panel: radial profiles of Sérsic images and their convolution with a point-symmetric Gaussian image with σ equal to 1/40 of the half-light radius of the Sérsic model. Dashed lines and diamonds show the case of a circular Sérsic image; the solid lines and rectangles are for an elliptical Sérsic image (ellipticity $= 1 - b/a = 0.4$). The red lines are the unconvolved Sérsic models. The black symbols are the results of one-dimensional convolution (Equations (6)–(8)) and the blue lines are the radial profiles of the convolved images, derived using ellipse-fitting. Bottom panel: the flux ratio or the difference in surface brightness (μ) between the one-dimensionally convolved Sérsic profile (I_{1D} or μ_{1D}) and the radial profile of the convolved Sérsic image (I_{2D} or μ_{2D}) for both the circular and elliptical cases.

A1836-BCG, IC 4296, NGC 3607, NGC 5128, and NGC 7052 makes it very difficult to robustly compute the core properties, so these galaxies are not included. NGC 4473 has been shown not to be a core galaxy by Ferrarese et al. (2006), KFCB09, and Dullo & Graham (2012, 2013), while the same is true for NGC 5576 (Trujillo et al. 2004); see also Dullo & Graham (2013). In addition, Trujillo et al. (2004) were only able to classify NGC 5077 as a "possible core" galaxy, so we exclude it as well. NGC 524 is a particularly problematic case, since there is evidence for very complex morphology—e.g., Laurikainen et al. (2010) fit a ground-based image using a Sérsic bulge, an exponential disk, and two "lens" components. This means that a simple core-Sérsic fit—or even core-Sérsic + outer envelope, as we use for some galaxies—is probably not appropriate. In addition, the best available high-resolution data is *HST*-NICMOS2, and the fit to this data by Richings et al. (2011) suggests a core break radius $r_b \sim 0\farcs18$, which is smaller than our adopted resolution limit for NICMOS2 data (see Section 2.1). (WFPC2 images are not usable due to the extensive circumnuclear dust lanes.) We reluctantly exclude this galaxy as well.

NGC 1374 represents a case where the core detection is ambiguous, so it is discussed independently in a separate section. This galaxy was classified as a non-core galaxy in Dullo & Graham (2012) using a limited data set from L05, and also by Dullo & Graham (2013) using a more extended ACS-WFC profile from Turner et al. (2012); in Section 3.2 we show the fit using our surface brightness profile which is slightly more extended in radius and which does not suffer the possible sky-subtraction uncertainties of the ACS-only Turner et al. data (see the discussion in Paper I). Table 2 summarizes the list of galaxies for which the presence of a core is confirmed. The best-fitting core-Sérsic parameters are also given in the same table. The best-fit Sérsic and core-Sérsic functions of these galaxies are shown in Figure 2 and the criteria which lead to the core identification are discussed below.

3.1. The Core Galaxies

When possible, we use all the available data points in the fitting. For all galaxies, the core-Sérsic function gives a much better fit to the whole profile than the Sérsic. In several galaxies, however, we find that the fit residuals become rather large at several outermost data points. Since these data points do not seem to be well-described by a Sérsic function, they are excluded from the fit. We keep only the data points where the fit residual is less than 0.15 mag. The deviation from the Sérsic model at large radii by more than 0.15 mag may be caused by imperfect sky subtraction or it may represent a real departure from the Sérsic profile, for example when an outer halo is present; see Section 4 for details on fits using extra components. The fit is then repeated using only the remaining data points, after excluding the outliers. The fit residuals, their rms, and the χ^2 values are presented in Figure 2. In this figure, the surface brightness profiles shown are not corrected for Galactic extinction.

In all the galaxies in Figure 2 we see a pattern in the residuals of the Sérsic fit that qualitatively suggests the presence of the core—compare to Figure 3 in Trujillo et al. (2004). This residual pattern disappears when the galaxy is fitted with the core-Sérsic profile. So the first criterion in Section 2.1 is secured. In each case, the rms of the residuals for the best Sérsic fit is much larger than that for the core-Sérsic. The χ^2 values for each galaxy are calculated by adopting the residual rms of the best core-Sérsic fit as the error on the surface brightness measurements. As discussed in KFCB09, this estimate for the real error is reasonable as long as the rms is of the order of the profile measurement error, i.e., a few hundredths of a mag arcsec^{-2}, which is indeed the case for all the galaxies that we examine. Using this error approximation, the χ^2 of the core-Sérsic fit is artificially set to 1.0. Note that the rms and χ^2 values are dependent on the radial extent and the radial sampling (logarithmic sampling is used here). We find that the (reduced) χ^2 value for each Sérsic fit is much more than twice that of the core-Sérsic. The average ratio of χ^2_S/χ^2_{CS} is around 49, with a minimum of 6.8, easily fulfilling the second criterion. To assess the third criterion, one can compare the position of the second innermost data point to the position of the dotted vertical line which marks the break radius. It is thus clear that we have cases of resolved cores. The fourth point is also satisfied, since inside the break radius the core-Sérsic function shows a consistent deficit in light compared to the extrapolated Sérsic profile (shown by the blue line). For the cases where we exclude some data points, the core is already well identified when fitting all the data points, i.e., fulfilling the four criteria simultaneously. Limiting the fitting range only improves the distinction. Lastly, the break radius for each galaxy is larger than twice the FWHM of the imaging data used to construct the innermost part of the surface brightness profile, described more quantitatively in Section 2.1.

Among the 23 galaxies, several exhibit more complex structures. Inside $\sim 0\farcs7$, the surface brightness profile of IC 1459 seems to show a small excess of light. We model this nuclear excess as an extra Gaussian component in the center on top of the core-Sérsic function, which after PSF convolution provides a good fit to the data. (In the cases of NGC 1407 and NGC 4552, it is not clear that their inner excesses can be

Table 2
The Core Sample: The core-Sérsic Function Parameters

Galaxy	n	μ_b (mag arcsec^{-2})	r_b ($''$)	r_e ($''$)	α	γ
IC 1459	7.62 ± 0.89	15.53 ± 0.08	0.69 ± 0.07	45.43 ± 4.87	1.39 ± 0.12	0.13 ± 0.04
NGC 1399*	7.38 ± 0.41	17.92 ± 0.02	2.47 ± 0.05	36.20 ± 0.67	1.93 ± 0.09	0.12 ± 0.01
NGC 1407*	2.17 ± 0.18	18.37 ± 0.01	2.01 ± 0.06	9.35 ± 0.69	3.80 ± 0.17	0.16 ± 0.00
NGC 1550	7.96 ± 0.24	16.48 ± 0.07	1.19 ± 0.09	39.08 ± 1.24	5.24 ± 1.78	0.52 ± 0.05
NGC 3091	9.29 ± 0.57	15.13 ± 0.05	0.62 ± 0.04	91.01 ± 11.07	1.90 ± 0.19	0.13 ± 0.05
NGC 3379	5.80 ± 0.10	14.40 ± 0.02	1.09 ± 0.04	55.14 ± 0.87	2.52 ± 0.16	0.22 ± 0.01
NGC 3608	6.29 ± 0.07	15.11 ± 0.07	0.21 ± 0.02	56.92 ± 1.36	4.14 ± 1.32	0.28 ± 0.05
NGC 3842	6.27 ± 0.18	17.42 ± 0.03	0.70 ± 0.03	58.75 ± 2.89	5.08 ± 2.21	0.19 ± 0.01
NGC 4261	6.33 ± 0.16	16.65 ± 0.03	1.18 ± 0.05	77.10 ± 2.56	3.78 ± 0.58	0.07 ± 0.03
NGC 4291	5.63 ± 0.06	15.17 ± 0.02	0.33 ± 0.01	15.35 ± 0.14	3.60 ± 0.28	0.10 ± 0.02
NGC 4374	7.06 ± 0.23	16.12 ± 0.04	1.47 ± 0.07	126.17 ± 5.30	3.41 ± 0.51	0.14 ± 0.02
NGC 4472	5.60 ± 0.09	16.48 ± 0.03	1.82 ± 0.09	199.13 ± 3.84	3.05 ± 0.38	0.06 ± 0.02
NGC 4486	8.91 ± 0.44	18.06 ± 0.04	8.14 ± 0.29	180.85 ± 4.13	2.13 ± 0.14	0.23 ± 0.01
NGC 4552*	3.82 ± 0.40	15.03 ± 0.06	0.34 ± 0.02	19.80 ± 1.92	7.00 ± 3.16	0.03 ± 0.04
NGC 4649	5.90 ± 0.13	16.84 ± 0.02	2.86 ± 0.09	124.54 ± 2.70	3.34 ± 0.43	0.19 ± 0.01
NGC 4889	9.78 ± 0.36	17.19 ± 0.03	1.58 ± 0.05	169.24 ± 14.76	4.82 ± 0.42	0.11 ± 0.01
NGC 5328	11.13 ± 0.45	17.07 ± 0.04	0.85 ± 0.04	76.84 ± 5.57	2.54 ± 0.22	0.07 ± 0.05
NGC 5516*	6.34 ± 0.90	16.39 ± 0.04	0.61 ± 0.03	24.22 ± 7.02	2.04 ± 0.15	0.12 ± 0.02
NGC 5813*	2.07 ± 0.04	15.25 ± 0.02	0.35 ± 0.01	3.49 ± 0.03	2.81 ± 0.26	0.0 ± 0.0
NGC 5846	5.32 ± 0.10	16.36 ± 0.03	1.24 ± 0.04	113.15 ± 2.82	3.25 ± 0.30	0.0 ± 0.0
NGC 6086*	3.13 ± 0.36	17.12 ± 0.04	0.55 ± 0.02	3.19 ± 0.58	3.44 ± 0.27	0.12 ± 0.01
NGC 7619	9.32 ± 0.36	14.90 ± 0.09	0.48 ± 0.06	100.06 ± 6.12	1.51 ± 0.12	0.14 ± 0.07
NGC 7768	6.15 ± 0.07	16.80 ± 0.03	0.29 ± 0.01	46.07 ± 1.12	100.0	0.21 ± 0.02

Notes. These parameters correspond to the best-fitting core-Sérsic models plotted in Figure 2. Asterisks indicate galaxies that were fit using multiple components (see Section 4). For these galaxies, we list parameters for the central (core-Sérsic) component; see Table 3 for the parameters of the outer components. The surface brightness profiles are calibrated to different bands, indicated in the *y*-axis title of the corresponding plots (see also Table 1); μ_b values are not corrected for extinction. The uncertainties are calculated from 100 Monte Carlo realizations, described in Section 6. The α parameter in NGC 7768 is fixed to 100.0 as an approximation to $\alpha = \infty$ (see the text).

Table 3
Parameters of Outer Sérsic Components in Multi-component Galaxies

Galaxy	Band	n	μ_e (mag arcsec^{-2})	r_e ($''$)
NGC 1399	*B*	1.33	25.08	189.5
NGC 1407	*B*	0.44	22.96	27.0
NGC 1407	*B*	1.25	23.95	112.7
NGC 4552	*V*	2.02	25.04	222.0
NGC 5516	*R*	1.33	25.08	189.5
NGC 5813	*i*	0.77	23.73	57.2
NGC 6086	*R*	2.06	24.25	50.8

Notes. Parameters of the outer envelope (Sérsic) component for the six galaxies which we fit with core-Sérsic plus an outer envelope. NGC 1407 is fit with *two* outer Sérsic components; the NGC 1399 fit also includes an outer exponential with $\mu_0 = 25.93$ and scale length $h = 1012''.4$.

modeled with a Gaussian, so we exclude the data at $r < 0''.16$ for NGC 1407 and $r < 0''.04$ for NGC 4552.) For six galaxies (including NGC 1407), we find that significantly better fits are achieved by including one or two extra Sérsic or exponential components, representing outer halos. This approach is discussed in more detail in Section 4.

The parameter values of the best-fit core-Sérsic model for each galaxy are provided in Table 2. The uncertainties of the core-Sérsic parameters are determined through a Monte Carlo simulation (see the next section). The Sérsic indices for these galaxies are almost all larger than 4, something that is common for giant ellipticals (e.g., Caon et al. 1993; KFCB09). The exceptions are four of the galaxies which we model with multiple components (see Section 4). The best-fit α parameter for NGC 7768 is found to be 16.6. This large value indicates a very sharp transition between the Sérsic and the power-law profile. When the fit is repeated with $\alpha = 100$, which is a good approximation for $\alpha = \infty$ (Graham et al. 2003), the best-fit values for the other five parameters hardly change. Since for large α (>10) the profile becomes insensitive to the exact value of α, we prefer to use the latter fit (fixing α to 100) to the light profile of NGC 7768. This choice prevents wildly varying values of α that are not physically meaningful in the Monte Carlo simulations.

For six galaxies whose surface brightness profiles are taken from KFCB09 (i.e., NGC 4261, NGC 4374, NGC 4472, NGC 4486, NGC 4552, and NGC 4649), the best-fitting Sérsic model of KFCB09 is also overplotted on the right-hand panels of Figure 2. Our inward-extrapolated Sérsic components and their Sérsic fits do not coincide, reflecting the differences in the way the core is defined. Note that KFCB09 use major-axis profiles while we use circularized profiles, resulting in a seemingly poorer fit of KFCB's Sérsic models in Figure 2. For a more thorough comparison between our and their fitting procedure, see Appendix M.

NGC 3091 and NGC 7619 show small values in α, i.e., $\alpha < 2$. Dullo & Graham (2012) produce a best-fitting core-Sérsic model of NGC 7619 by keeping α constant at 5, which enforces a rather sharp transition from Sérsic to power-law profiles. Doing this exercise using our circularized profile of NGC 7619 results in a smaller n (7.71), larger r_b ($0''.73$) and γ (0.47), and a larger rms (0.033). It is worth emphasizing that Dullo & Graham (2012)'s profile for NGC 7619 is not as extended as ours and stops short of $r \approx 20''$.

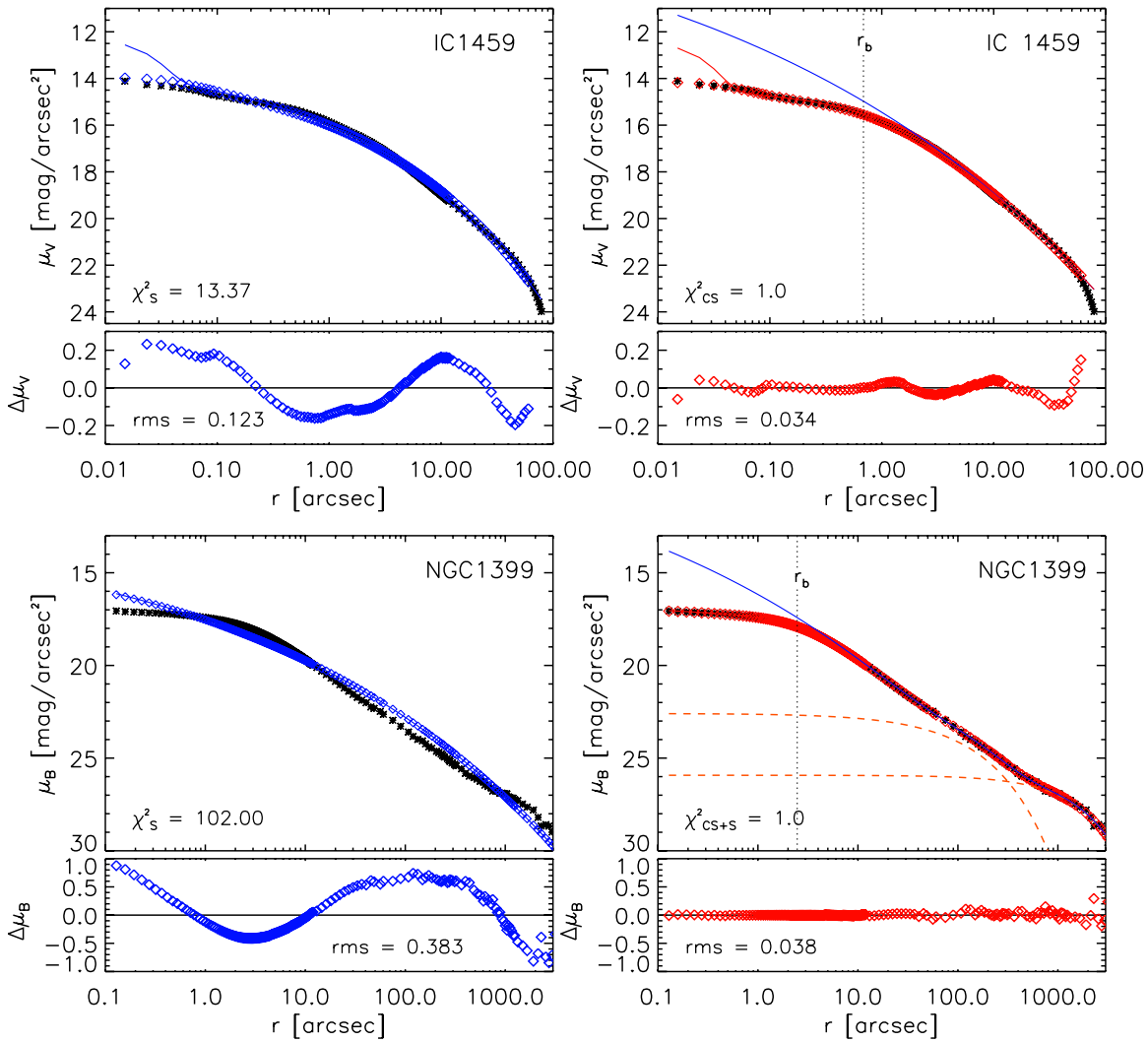

Figure 2. Model fits to the surface brightness profiles of all the galaxies in Table 1, except for NGC 1374 (each row for each galaxy). The small lower panel of each plot shows the residual profile, i.e., the difference between the convolved best-fit model and the observed profile. In the left column, we show the Sérsic fit. The black asterisks show the observed profile, the blue diamonds in the upper panels are the convolved best-fit Sérsic function, and the blue line is the intrinsic Sérsic function (before PSF convolution). In the right column, we show the core-Sérsic (or core-Sérsic + envelope) fit. The red diamonds in the upper panels are the convolved best-fit core-Sérsic (+ envelope) function, the solid red line shows the intrinsic function (before PSF convolution), and the blue line is the inward extrapolation of the outer, Sérsic part of the core-Sérsic function. For fits with an outer envelope, the dashed red lines indicate the envelope components by themselves. The diamonds coincide exactly with the lines of the same color for galaxies whose light profile is derived from a deconvolved image, since there is no PSF convolution in the fit. The vertical dotted lines mark the break radius (r_b). The rms of each Sérsic and core-Sérsic (+ envelope) fit is shown and the latter is taken as the uncertainty in the surface brightness profile, thereby setting the χ^2 value of the core-Sérsic (+ envelope) fit to 1.0. The fit range is limited to a certain radius for several galaxies (see the text). For galaxies with profiles taken from KFCB09, a green dashed line is plotted based on the Sérsic function that best fits the outer part of the galaxy according to KFCB09. For IC 1459, an additional Gaussian component is included in the fits to account for excess nuclear light.

(An extended, color version of this figure is available in the online journal.)

3.2. NGC 1374

NGC 1374 is the one galaxy in the sample of Paper I with conflicting arguments about the existence of a core. L05 classify NGC 1374 as a core galaxy, based on a Nuker profile fit to their *HST* imaging data. Dullo & Graham (2012), however, do not confirm the core in this galaxy using the same data, and Dullo & Graham (2013) come to the same no-core conclusion using a more extended ACS-WFC-based profile from Turner et al. (2012). In contrast, Lauer (2012) argues for the presence of the core.

From fitting core-Sérsic models to our data, we find no solid evidence that a core is present in this galaxy. We tested different fitting ranges by varying the maximum radii of the fitted data point, but there is no strong visibility of a core in any case. In the top row of Figure 3, we show the Sérsic and core-Sérsic fits to the whole profile and to a limited profile. For the latter, we limit the fitting range to $r < 7''$ (for a fair comparison to the fitting using L05 data, see below). Judging by eye, there is no significant difference in fit quality between the Sérsic and the core-Sérsic profiles, although the overall residual rms and χ^2 of the core-Sérsic are smaller and $\chi^2_S > 2\chi^2_{CS}$. When fitting the whole range, the Sérsic profile actually provides a better fit in the center and instead of seeing a core, the core-Sérsic fit indicates an extra light on top of the Sérsic component (this might be consistent with the extra nuclear component used by Dullo & Graham 2012, 2013 in their fits to this galaxy). There is a slight improvement and a vague indication of a core when we fit only up to $7''$. However, if we base our core classification on Trujillo et al. (2004)'s criteria, this fit fails at the second criterion.

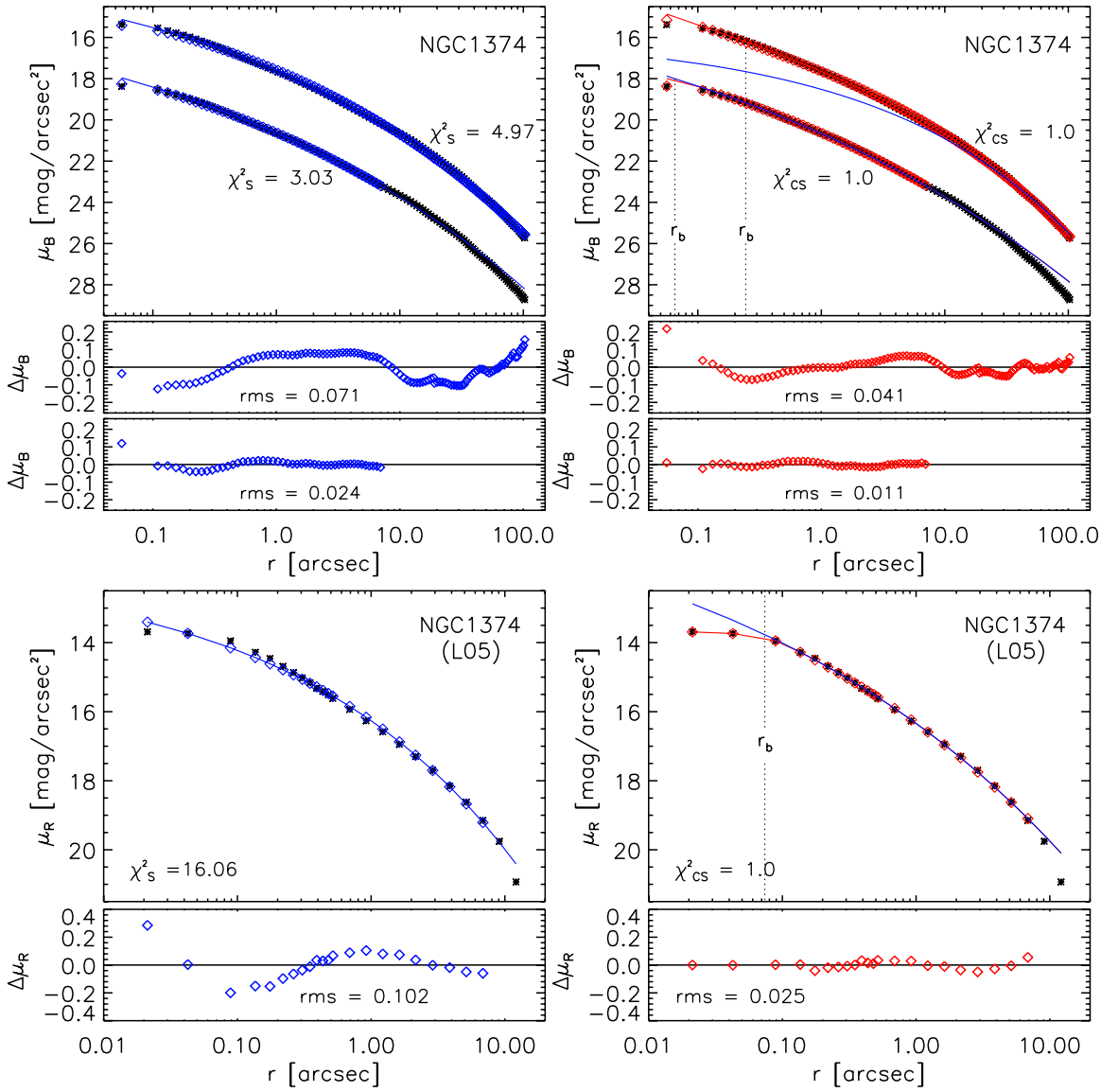

Figure 3. Model fits to the surface brightness profiles of NGC 1374. Top row: model fits to the surface brightness profile derived in Paper I. On the left side, we show the Sérsic fit to all the data points (upper profile) and the Sérsic fit only to data points with $r < 7''$ (shifted 3 mag down for clarity). The black asterisks show the observed profile, the blue diamonds are the convolved best-fit Sérsic model, and the blue line marks the intrinsic Sérsic model (before PSF convolution). The upper black asterisks show the actual values of surface brightness. The middle and bottom panels show the residuals for the fit to all data points and for the fit to $r < 7''$, respectively. The right-hand set of panels shows the same thing for the core-Sérsic fits. The red diamonds are the convolved best-fit core-Sérsic model, the red line shows the intrinsic core-Sérsic model (before PSF convolution), and the blue lines are the Sérsic model that fits only the outer part of the galaxies. Bottom row: model fits to the surface brightness profile reported in L05. The fit is done for $r < 7''$. The vertical dotted and dashed lines mark the break radius (r_b) and the radius at which the core-Sérsic model deviates from the extrapolated Sérsic model by more than the rms of the residuals ($r_{\rm rms}$). Note that the diamonds and the line with the corresponding color coincide with each other, since there is no PSF convolution.

(A color version of this figure is available in the online journal.)

Our next attempt is to fit the data of L05 to confirm or reject their finding. Their profile has been corrected for the PSF effect, so we directly fit it with the models without convolution. As shown in Figure 3, we detect a core in this galaxy, albeit weak, by discarding the two outermost data points ($r > 7''$). Extending the fitting range of data does not give the same results, i.e., the existence of the core becomes inconclusive and the core disappears altogether when all the data points are included in the fit. L05 fit their light profile with a Nuker model and it appears that they also made the compromise of neglecting the 3–4 last data points in the fit, in order to detect the core. Moreover, our best-fitting break radius is smaller than $0\farcs1$, less than the inner resolution limit that we adopt as an additional criterion of core detection in Section 2.1.

One might conclude that our data lack spatial resolution and that this situation is aggravated by the PSF convolution in the fitting process. It is, however, important to note that the core disappears when extended data points are included in either our profile or the L05 profile. Graham et al. (2003) pointed out that fitting a Nuker model to a limited light profile, such as the case of NGC 1374 in L05, could lead to a false conclusion that a core exists. Having no definite evidence of a depleted core in NGC 1374, we exclude it from the core sample.

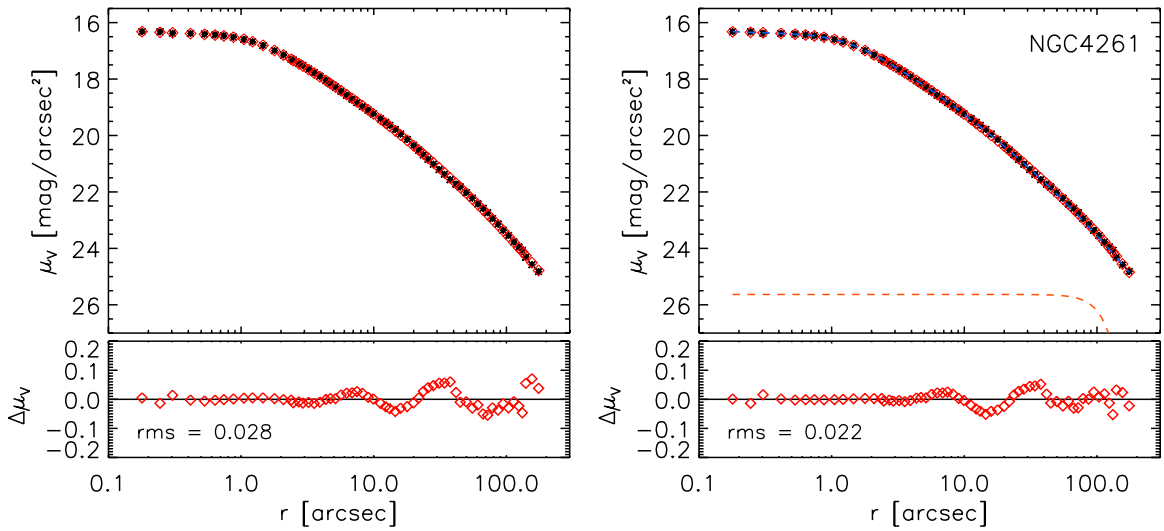

Figure 4. Example of a galaxy (NGC 4261) where the preferred fit is a simple core-Sérsic. Left: best-fitting core-Sérsic model (red diamonds) compared to the data (black asterisks). Right: same profile, but now with the best-fitting sum of a core-Sérsic (dashed blue line) and a Sérsic profile. The Sérsic profile (dashed red line) is everywhere much fainter than the core-Sérsic profile, so that the latter is almost identical to the result of fitting a single core-Sérsic function by itself. The majority of galaxies in our sample are similar to this, with little or no evidence for a significant outer envelope in addition to the core-Sérsic profile.

4. FITTING GALAXY PROFILES WITH MULTIPLE COMPONENTS

While the current paradigm for elliptical galaxies is that their surface brightness profiles (outside of the nuclear region) are best fit with the Sérsic function, there are also long-standing arguments that at least *some* elliptical galaxies may have light at large radii attributable to an extra component. In particular, several studies have shown that BCGs, including but not limited to cD galaxies, are better fit with a combination of two profiles: an inner Sérsic (or $r^{(1/4)}$) function plus an outer envelope, the latter modeled with exponential, $r^{(1/4)}$, or Sérsic functions (e.g., Gonzalez et al. 2003, 2005; Seigar et al. 2007; Donzelli et al. 2011). Hopkins et al. (2009) have shown that a plausible outcome of mergers is an outer Sérsic profile plus an inner, exponential-like excess due to central, post-merger starbursts; such multi-component profiles could persist even after "a moderate number" of subsequent dry mergers. They suggested that modeling core-galaxy profiles with single components (such as the core-Sérsic profile) could result in biased estimates of the core light and mass deficits; one possible signature of this is Sérsic or core-Sérsic fits with large values of n. Donzelli et al. (2011) noted that those BCGs that were best fit with two-component profiles had, when fit with just a single Sérsic function, large values of n and r_e (>8 and >300 kpc, respectively). Most recently, Huang et al. (2013) have argued, using 2D fits to ground-based images, that many ellipticals may be better modeled as the sum of *three* (or in some cases even *four*) Sérsic functions.

Some of the galaxies in our sample are BCGs (e.g., NGC 4472 and NGC 6086), which suggests that we should consider the possibility of outer envelopes. In addition, some of our core-Sérsic fits to the surface brightness profiles (including both BCG and non-BCG galaxies) resulted in very large values of the index n (e.g., $n > 10$ or even 20) and/or the effective radius r_e (e.g., $r_e \gg$ radius of outermost data point). To investigate the possibility of outer envelopes, we re-fit *all* the galaxies in our sample (excepting NGC 1374, which we judged to not be a core galaxy) using the sum of a core-Sérsic and an extra Sérsic profile. In the majority of cases, the result was essentially identical to fitting the profile with just a single-core-Sérsic component, with the extra Sérsic component producing minimal contribution at all radii, and the parameters of the core-Sérsic component changing very little (e.g., mean change in $r_b \approx 11\%$); see Figure 4 for an example. Galaxies for which the fit was notably improved—with the outer component contributing the majority of light at the largest radii—were almost always cases where the single-core-Sérsic fit had excessively large values of n and/or r_e (see Figure 5).

In order to decide which galaxies were most plausibly better fit by a multi-component profile, we adopted the following set of conditions for using a multi-component fit in place of a single-core-Sérsic fit. If at least one of the following is true, then we use the multi-component fit instead of the core-Sérsic fit.

1. The index n of the single-core-Sérsic fit is >10, *and* the multi-component fit has core-Sérsic and Sérsic indices <10. (See Figure 5 for an example.)
2. The effective radius r_e of the single-core-Sérsic fit is $>$ the radius of the outermost fitted data point, *and* the reverse is true for the multi-component fit.
3. The rms of the multi-component fit is at least four times smaller than the rms of the single-core-Sérsic fit.

In the end we found that approximately one-fourth of our sample galaxies were best fit using multiple components: NGC 1399, NGC 1407, NGC 4552, NGC 5516, NGC 5813, and NGC 6086. The first two galaxies were special cases where fitting the envelope required *two* additional components. For NGC 1399, we used the sum of a Sérsic and an exponential, while for NGC 1407 we used the sum of two Sérsic functions. In at least two cases—NGC 5813 and NGC 6086—we can plausibly associate the outer Sérsic component with outer isophotes which are significantly more elliptical than the inner part of the galaxy (where the core-Sérsic component dominates the light).

What is the effect of using multiple-component fits on the core properties? On average, the derived core sizes (r_b of the core-Sérsic component) are $\sim$10%–15% smaller when multiple components are used. Using multiple-component fits has a stronger effect on the estimated light and mass deficits (see

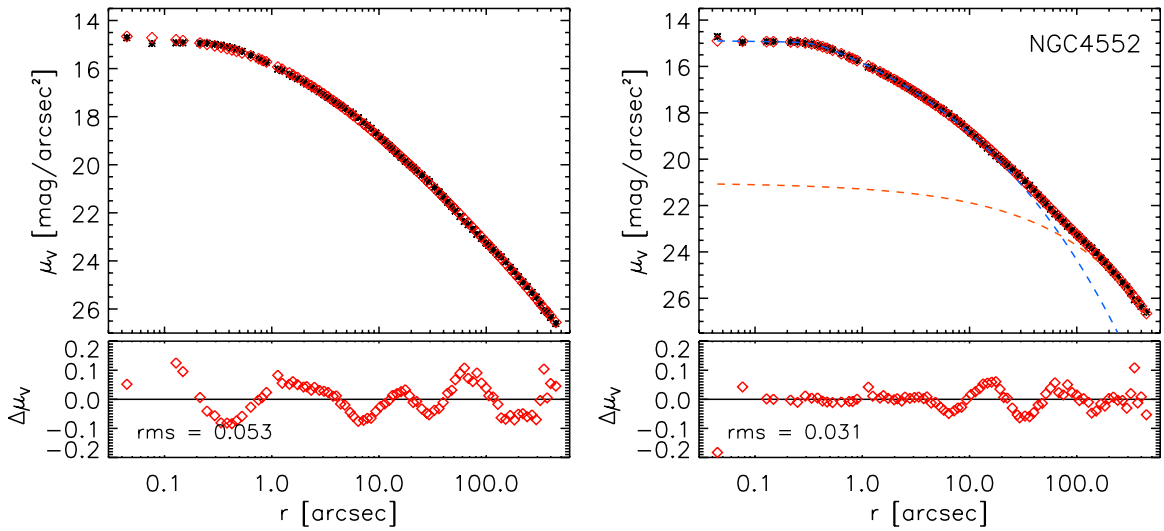

Figure 5. As for Figure 4, but now showing a galaxy (NGC 4552) where we adopt a multi-component fit as the best fit to the surface brightness profile. Left: best-fitting core-Sérsic fit (red diamonds) and data (black asterisks). This core-Sérsic fit has an unusually large value of n (13.9). Right: same data, but now showing the best-fitting sum of a core-Sérsic and a Sérsic profile. The core-Sérsic component (dashed blue line) now has $n = 3.8$; the outer Sérsic component (dashed red line) has $n = 2.0$. The residuals are smaller as well, including those in the core region.

(A color version of this figure is available in the online journal.)

Section 6). The most common effect is to lower the estimated deficit (the median deficit is 0.44 times what it is when a single-core-Sérsic fit is used), with an extreme in the case of NGC 4552, for which the deficit is only 0.9% of the value for the single-core-Sérsic fit. For two galaxies (NGC 1399 and NGC 5516), on the other hand, the deficit roughly doubles in size.

5. COMPARISON WITH PREVIOUS CORE-SÉRSIC FITS

Several previous studies have performed core-Sérsic fits to the surface brightness profiles of some of our galaxies. The main relevant studies are those of Ferrarese et al. (2006), Richings et al. (2011), and Dullo & Graham (2012). We concentrate on values of the break radius r_b and the index n describing the curvature of the profile outside of the core, since these are reported by all three studies.[5]

The left panel of Figure 6 compares r_b values from the various studies with those from our fits. The agreement is generally excellent; a correlation analysis shows that the r_b values from all three studies are well correlated with our values for galaxies in common: Spearman $r_s = 1.0$, 0.97, and 0.96 for the Ferrarese et al. (2006), Richings et al. (2011), and Dullo & Graham (2012) values, respectively, compared to ours (the corresponding probabilities are 0.0, 2.2×10^{-5}, and 7.3×10^{-6}). The Ferrarese et al. (2006) break radii are on average 1.20 ± 0.43 times ours (median = 1.07), the Richings et al. (2011) values are 1.23 ± 0.39 times ours (median = 1.09), and the Dullo & Graham (2012) values are 0.99 ± 0.14 times ours (median = 1.01), so there is no clear evidence for systematic offsets or biases between the different studies when it comes to the break radius.

The right panel of Figure 6 compares the n values of the various core-Sérsic fits with ours. Here, the agreement is clearly much worse, and there are hints of possible systematic bias: the previous measurements tend to be *lower* than our values of n. The Ferrarese et al. (2006) values are a median of 0.98 times ours (mean = 1.07 ± 0.46), while the values for Richings et al. (2011) and Dullo & Graham (2012) are 0.71 (mean = 1.12 ± 1.21) and 0.81 (mean = 0.89 ± 0.43), respectively. Six of the nine Richings et al. and eight of the ten Dullo & Graham n values are lower than ours, though this is not a statistically significant bias. More generally, we can note that a correlation analysis shows almost no agreement between the various values of n: $r_s = 0.10$, -0.13, and 0.09 ($P = 0.87$, 0.73, and 0.81) for the Ferrarese et al., Richings et al., and Dullo & Graham measurements compared to ours. In addition, a Kolmogorov–Smirnov (K-S) test suggests that the Dullo & Graham n values, and possibly the Ferrarese et al. values as well, are drawn from different distributions than ours ($P = 0.0069$ and 0.031).

While it is true that some of our profiles are fit with a different model—core-Sérsic + outer envelope(s) instead of just a core-Sérsic function—this is true for only one-fourth of our total sample and cannot be the cause of the discrepancy. If we exclude those galaxies in common with the other studies for which we use multi-component fits (NGC 1399, NGC 4552, and NGC 5813), the correlations and K-S test results do not improve: the correlation coefficients become $r_s = 0.60$, -0.14, and -0.071 for the three studies, with $P = 0.40$, 0.76, and 0.88, while the K-S test probabilities become 0.53, 0.13, and 0.0042. This might seem to suggest that the Ferrarese et al. values have the best agreement with ours, but there are only four galaxies in common when we exclude our multi-component fits, so we really cannot make that conclusion.

We suspect that the main reason for the poor agreement between previous measurements of core-Sérsic n and ours for these galaxies is the much smaller radial range of the surface brightness profiles used in the previous studies. Both Richings et al. (2011) and Dullo & Graham (2012) use profiles that extend to only ~10–15″, which means that the outer Sérsic part of the core-Sérsic profile is poorly constrained. Even though the galaxies from Ferrarese et al. (2006) have profiles which extend to $r \sim 100''$, our profiles for the same galaxies extend to 4–7 times further out in radius. Note that for six galaxies we used profiles from Kormendy et al. (2009). Their Sérsic n measurements agree well with our values (at the $1.4\,\sigma$ level on average, having excluded NGC 4552, where we adopt a two-component fit).

An additional factor might be sky-subtraction errors. For example, Dullo & Graham (2012) used profiles originally

[5] Dullo & Graham (2012) do not report r_e values for their fits.

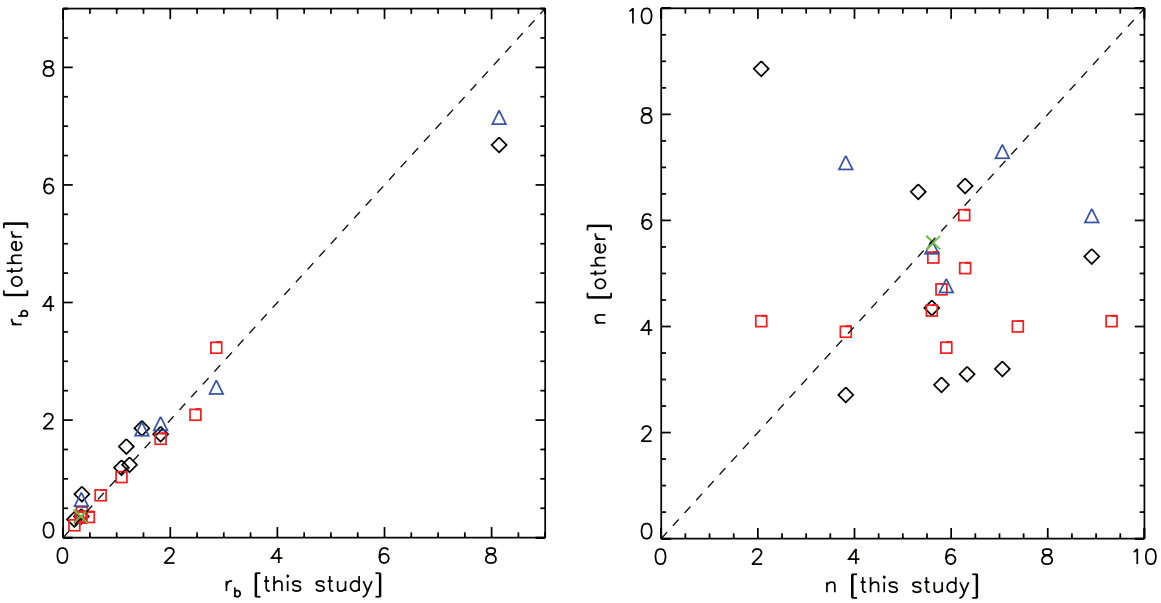

Figure 6. Left panel: comparison of literature values of r_b from core-Sérsic fits to galaxies in our sample, using results from Ferrarese et al. (2006, blue triangles), Richings et al. (2011, open black diamonds), and Dullo & Graham (2012, red squares); the green X is NGC 4291 from Trujillo et al. (2004). Right panel: same, but now comparing values of the core-Sérsic index n.

(A color version of this figure is available in the online journal.)

published by L05. These profiles were extracted from the PC chip of the *HST* WFPC2 array, and a sky subtraction was applied using measurements made in the far corners of the WF3 chip. Since almost all of these galaxies are larger than the WFPC2 array—sometimes much larger (e.g., NGC 1399)—this "sky" measurement will necessarily include some galaxy light, and thus the resulting profile will be over-subtracted. Over-subtracted profiles decline more steeply at large radii, and are better fit by Sérsic profiles with lower values of n.[6]

It is clear from this comparison that the outer part of the core-Sérsic fit is sensitive to how far out the surface brightness profile extends; fits to profiles which only extend to $\sim 10''$ are likely to be poorly constrained when it comes to the values of n. It is important to note that the *core* parameters are much more robust: the size of the break radius is relatively insensitive to how much of the outer profile is included in the fit.

6. THE LIGHT AND MASS DEFICIT IN THE CORE

We define the light deficit in the inner part of the galaxy as the difference between the luminosity of the Sérsic component of the best-fitting core-Sérsic model and the luminosity of the core-Sérsic model itself; both are integrated out to the radius of the last data point. (For galaxies with multiple-component fits, we consider only the core-Sérsic component and ignore the outer envelope.) Since this radius is much larger than the break radius, the difference represents the total light deficit and is independent of the choice of the maximum radius.

We first calculate intensity in the units of solar luminosity per pc^2 from the surface brightness μ (mag arcsec^{-2}):

$$I(L_\odot/\mathrm{pc}^2) = (206265)^2 \times 10^{0.4(M_{\rm sun}-\mu-5)} \quad (9)$$

$$= 4.255 \times 10^8 \times 10^{0.4(M_{\rm sun}-\mu)}, \quad (10)$$

where $M_{\rm sun}$ is the absolute magnitude of the sun in the same band as μ. We then obtain the luminosity L interior to the last data point $r_{\rm last}$ by numerically integrating the intensity over a projected area $\pi\, r_{\rm last}^2$:

$$L(r \leqslant r_{\rm last}) = \int_0^{r_{\rm last}} I(r)\, 2\pi\, r dr. \quad (11)$$

This is calculated for both the core-Sérsic model and the extrapolated Sérsic component of that model. The difference between the two is the luminosity deficit ΔL (in $L_\odot$). For comparison with the work of KB09, the light deficit is computed in magnitudes according to $M_{\lambda,\rm def} = -2.5 \times \log_{10}(\Delta L) + M_{\rm sun}$, where λ indicates that the conversion is done in the same band. In order to convert the light deficit into a stellar mass deficit $M_{\star,\rm def}$, we use the stellar mass-to-light-ratio $\Upsilon_{\star,\rm dyn}$ derived from dynamical models (see Table 1).

For 16 of the 20 galaxies with reliable black hole mass determinations, these $\Upsilon_{\star,\rm dyn}$ values stem from two-component models that fit simultaneously for the $\Upsilon_{\star,\rm dyn}$ which scales the light-density profile and for the parameterized dark-matter halo density distribution (in addition to the black hole mass, of course). For the remaining four galaxies—IC 1459, NGC 3379, NGC 4261, and NGC 4374 (along with the three objects with dubious black hole masses, which we do not use in our analyses)—the $\Upsilon_{\star,\rm dyn}$ values come from single-component dynamical modeling (i.e., without dark matter), so the true $\Upsilon_{\star,\rm dyn}$ could be overestimated by $\approx$20% (see Thomas et al. 2007). We prefer this approach to the use of stellar-population $\Upsilon_\star$ determinations, because of the uncertainty that affects the latter concerning the proper stellar initial mass function (IMF) to be used. The recent results of Thomas et al. (2011), Wegner et al. (2012), Cappellari et al. (2012, 2013), and Conroy & van Dokkum (2012) all show that the IMF may change as one goes from low- to high-velocity-dispersion ellipticals, from a Kroupa IMF to an IMF even "heavier" than Salpeter, but the scatter in this trend is too large to predict the IMF on the basis of the velocity dispersion; moreover, some high-dispersion ellipticals

[6] For the five Ferrarese et al. (2006) galaxies in common with our sample, sky subtraction was estimated based on the pointing of *HST*. Richings et al. (2011) provide no information as to what, if any, sky subtraction was done for their data.

Table 4
The Light and Mass Deficits in the Core

Galaxy	$M_{\lambda,\mathrm{def}}$ (mag)	Color	Value	$M_{V,\mathrm{def}}$ (mag)	$M_{\star,\mathrm{def}}$ ($M_\odot$)	$f(M_{\mathrm{BH}})$
IC 1459	-19.15 ± 0.35	...	...	-19.15 ± 0.35	$(1.78 \pm 0.75) \times 10^9$	0.64
NGC 1399	-18.37 ± 0.13	$B-V$	0.68	-19.05 ± 0.14	$(3.52 \pm 0.46) \times 10^{10}$	38.7
NGC 1407	-16.56 ± 0.17	$B-V$	0.98	-17.54 ± 0.18	$(4.31 \pm 0.92) \times 10^9$	0.96
NGC 1550	-19.17 ± 0.11	$V-R$	1.08	-18.09 ± 0.12	$(1.09 \pm 0.19) \times 10^{10}$	2.95
NGC 3091	-19.90 ± 0.20	$V-I$	1.39	-18.51 ± 0.21	$(1.57 \pm 0.34) \times 10^{10}$	4.37
NGC 3379	-17.56 ± 0.11	$V-I$	1.29	-16.27 ± 0.12	$(1.26 \pm 0.15) \times 10^9$	3.07
NGC 3608	-13.95 ± 0.10	...	...	-13.95 ± 0.10	$(1.01 \pm 0.13) \times 10^8$	0.21
NGC 3842	-17.88 ± 0.11	...	...	-17.88 ± 0.11	$(8.04 \pm 1.50) \times 10^9$	0.83
NGC 4261	-17.67 ± 0.12	...	...	-17.67 ± 0.12	$(9.11 \pm 1.58) \times 10^9$	17.5
NGC 4291	-15.92 ± 0.06	...	...	-15.92 ± 0.07	$(1.07 \pm 0.16) \times 10^9$	1.16
NGC 4374	-17.68 ± 0.15	...	...	-17.68 ± 0.15	$(6.85 \pm 1.10) \times 10^9$	7.45
NGC 4472	-17.35 ± 0.14	...	...	-17.35 ± 0.14	$(3.66 \pm 0.58) \times 10^9$	1.46
NGC 4486	-20.27 ± 0.16	...	...	-20.27 ± 0.16	$(6.76 \pm 1.34) \times 10^{10}$	10.9
NGC 4552	-14.12 ± 0.15	...	...	-14.12 ± 0.15	$(2.70 \pm 0.40) \times 10^8$	0.54
NGC 4649	-18.12 ± 0.12	...	...	-18.12 ± 0.12	$(1.11 \pm 0.17) \times 10^{10}$	2.22
NGC 4889	-20.62 ± 0.07	$V-R$	0.65	-19.97 ± 0.09	$(5.97 \pm 1.76) \times 10^{10}$	2.84
NGC 5328	-19.52 ± 0.09	...	...	-19.52 ± 0.09	$(2.70 \pm 0.41) \times 10^{10}$	6.23
NGC 5516	-19.12 ± 0.29	$V-R$	0.60	-18.52 ± 0.30	$(1.35 \pm 0.31) \times 10^{10}$	4.09
NGC 5813	-16.08 ± 0.22	$V-i$	0.71	-15.37 ± 0.24	$(5.80 \pm 1.24) \times 10^8$	0.83
NGC 5846	-17.48 ± 0.15	$V-i$	0.79	-16.69 ± 0.16	$(2.32 \pm 0.33) \times 10^9$	2.11
NGC 6086	-18.69 ± 0.20	$V-R$	0.60	-18.10 ± 0.21	$(7.36 \pm 1.70) \times 10^9$	2.05
NGC 7619	-20.05 ± 0.18	$V-I$	1.23	-18.82 ± 0.19	$(1.34 \pm 0.28) \times 10^{10}$	5.36
NGC 7768	-16.41 ± 0.06	...	...	-16.41 ± 0.06	$(2.46 \pm 0.50) \times 10^9$	1.89

Notes. $M_{\lambda,\mathrm{def}}$ is the absolute magnitude of the light deficit in the given filter (see Table 1). This quantity is converted to the V band ($M_{V,\mathrm{def}}$) using the color and its value in Columns 4 and 5. The value is specific for each galaxy and in general taken from Prugniel & Heraudeau (1998) for the smallest aperture available and then corrected for extinction (Schlegel et al. 1998); we assume a typical uncertainty of 0.05 mag for each color. For NGC 3091, I−F814W is 0.03 as derived in Paper I and for the extinction correction we adopt the value in the Landolt I band. For NGC 5813 and NGC 5846, the conversion from SDSS i band to Cousins I uses central $r-i$ colors measured from the SDSS images and the equations of Jordi et al. (2006), yielding $i-I=0.50$ for NGC 5813 and $i-I=0.51$ for NGC 5846. The uncertainty in the mass deficit $M_{\star,\mathrm{def}}$ takes into account the uncertainties in both the light deficit and $\Upsilon_{\star,\mathrm{dyn}}$.

may not have a "heavy" IMF (van den Bosch et al. 2012; Rusli et al. 2013; Smith & Lucey 2013). Possible spectroscopic information constraining the IMF (Conroy & van Dokkum 2012) is not available for most core galaxies. We apply a simple multiplication of $\Upsilon_{\star,\mathrm{dyn}} \times \Delta L$ (given that both are measured in the same band and assuming that $\Upsilon_{\star,\mathrm{dyn}}$ is constant within the galaxy) to obtain the mass deficit.

The uncertainties are calculated through a Monte Carlo simulation. Using the rms of the best fit as an estimate of the measurement error, Gaussian noise is added to the best-fit model profile to create 100 realizations of the observed surface brightness profile. For each realization, a best-fit core-Sérsic (or multiple-component) profile was derived and the light deficit was calculated in the same way as was done for the real profile. The rms of those 100 values of light deficit becomes the uncertainty. The error of the mass deficit is derived from the uncertainties of both the light deficit and $\Upsilon_{\star,\mathrm{dyn}}$. From these 100 realizations, we also derive the rms of each core-Sérsic parameter and adopt this as the error of the parameter (given in Table 2). This Monte Carlo approach provides estimates of random errors, not systematic errors. The latter could include errors in describing the PSF, errors in the sky subtraction, failure to account for possible substructure in the galaxies, and the sampling of the surface brightness profiles. One should also keep in mind that the circularized profiles that we use can be systematically different—depending on the ellipticity profiles—than the semimajor axis profiles commonly used in other papers.

To enable a statistical comparison of the light deficit $M_{\lambda,\mathrm{def}}$ among the galaxies, this quantity should be presented in a single photometric filter. For this purpose, we convert $M_{\lambda,\mathrm{def}}$ in the given band to the V band ($M_{V,\mathrm{def}}$) by applying a color correction based on a value obtained from the literature, specific for each galaxy. In the case where multiple aperture measurements are available, we take the color corresponding to the smallest aperture since we are mostly interested in the inner part of the galaxy where the core is present. We assume a typical uncertainty of 0.05 mag in color, taken into account in the error calculation for $M_{V,\mathrm{def}}$. Table 4 lists the color correction and the light and mass deficit for each galaxy.

7. BLACK HOLE–CORE CORRELATION

Taking the break radius (r_b) as a measure of the core size, we examine its relationships with galaxy velocity dispersion, luminosity, and the black hole mass. These are displayed in Figure 7. The fit to the data points (also for all the other fits in this section) is based on a Bayesian method with Gaussian errors and intrinsic scatter ϵ, described in Kelly (2007), and the results are shown by the black lines. For each diagram we perform non-symmetrical regression using either parameter to predict the other. We further compute the bisector of the two fitting results (with flipped x- and y-axes) to give a symmetrical representation of the correlation. The coefficients of the fits involving r_b are shown in Table 5. All the fits are linear fits to the logarithm of the relevant quantities expressed in the following form:

$$y = a + bx, \tag{12}$$

where y is $\log r_b$ (in kpc) and x is $\log \sigma_e/(200\ \mathrm{km\ s^{-1}})$, M_V, or $\log M_{\mathrm{BH}}/(3 \times 10^9 M_\odot)$. For the "direct" fits, σ_e, M_V, and M_{BH}

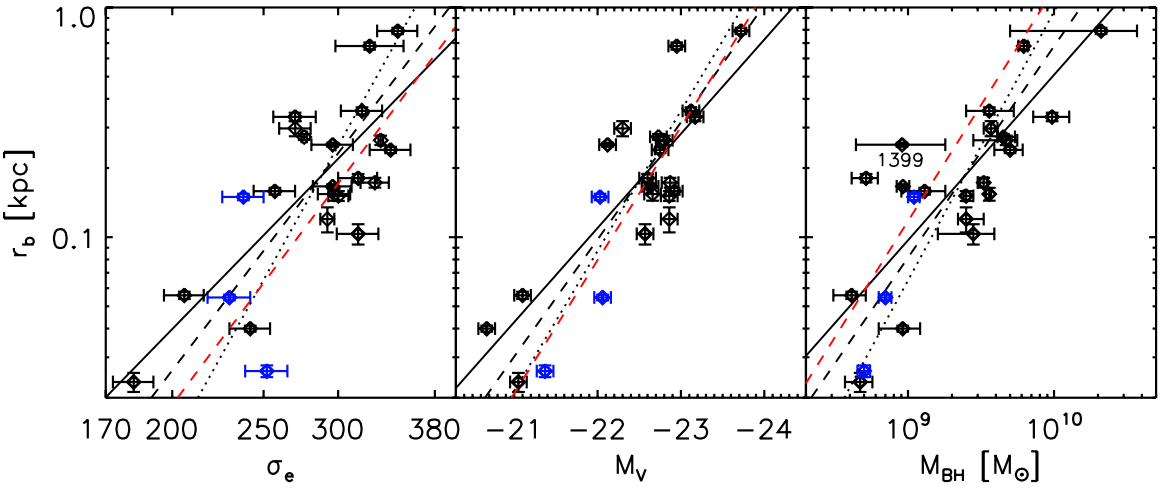

Figure 7. From left to right: the break radius is plotted as a function of velocity dispersion within the effective radius σ_e, luminosity of the host galaxy, and black hole mass. The 20 galaxies with reliable M_{BH} are represented by the black diamonds. The additional three galaxies without reliable M_{BH} (NGC 4552, NGC 5813, and NGC 5846) are shown in blue. The black lines show our fits to all black data points. The solid lines show the fits when x-axis variables are treated as independent variables/predictors, the dotted lines are fits when these parameters are the response, and the dashed lines represent the symmetrical bisector regression; see Table 5. The red dashed lines are the bisector fits from Dullo & Graham (2012), i.e., their Equations (5), (6), and (12), respectively.

(A color version of this figure is available in the online journal.)

Table 5
Relations between Core Size and Galaxy Parameters

Fit Type	a	b	ϵ	rms	r_s	P
		r_b vs. $(\sigma_e/200\ \mathrm{km\ s^{-1}})$			0.53	0.017
Direct	-1.41 ± 0.17	4.19 ± 1.00	0.27 ± 0.06	0.24		
Reverse	-1.84 ± 0.28	6.95 ± 1.71	0.34 ± 0.11	0.32		
Bisector	-1.57 ± 0.15	5.23 ± 0.96	0.30 ± 0.09	0.25		
		r_b vs. M_V			−0.65	0.0018
Direct	-0.55 ± 0.06	-0.41 ± 0.07	0.24 ± 0.05	0.20		
Reverse	-0.45 ± 0.09	-0.61 ± 0.13	0.29 ± 0.09	0.30		
Bisector	-0.50 ± 0.05	-0.51 ± 0.07	0.26 ± 0.07	0.22		
		r_b vs. $(M_{BH}/3 \times 10^9 M_\odot)$			0.77	7.3×10^{-5}
Direct	-0.68 ± 0.06	0.73 ± 0.16	0.25 ± 0.05	0.23		
Reverse	-0.64 ± 0.10	1.15 ± 0.37	0.32 ± 0.15	0.32		
Bisector	-0.66 ± 0.05	0.92 ± 0.17	0.28 ± 0.11	0.26		

Notes. Coefficients of fits between core size r_b (in kpc) and galaxy parameters (velocity dispersion, luminosity, or black hole mass) for the 20 core galaxies with well-determined black hole masses. For each relation we list intercept a, slope b, and intrinsic Gaussian scatter ϵ for direct, reverse, and bisector fits, along with the rms of residuals (in $\log r_b$) from the fit; see Section 7. The Spearman correlation coefficient r_s and its associated probability P are listed for each overall relation in the 6th and 7th columns.

are the independent variables in the fit, while in the "reverse" fits, r_b is the independent variable. The errors on the coefficient values are taken as the rms of the a posteriori parameter probability distribution. We also list the Spearman correlation coefficients and the corresponding probabilities for each relation in Table 5.

Dullo & Graham (2012) analyzed the same relationships using bisector fits. In the r_b–σ_e diagram, our fit predicts a slightly higher r_b for a given velocity dispersion, though the fits are compatible within the errors. In the r_b–M_V diagram, our fit coincides with their fit for high-luminosity galaxies ($M_V \gtrsim 23$). In the case of the r_b–M_{BH} relation, Graham & Dullo performed fits using both measured black hole masses (their Equation (12)) and proxy black hole masses estimated from the M_{BH}–σ and M_{BH}–L_V relations (their Equations (13) and (14)); only the former is actually plotted (their Figure 20). Since our fits use only measured black hole masses, we compare our results with their Equation (12) (lower right panel of Figure 6). For this relation, our fit suggests larger M_{BH} for the same value of break radius (or, conversely, smaller break radius for a given M_{BH}). We note that the fit in Dullo & Graham's Equation (12) is based on only 7 galaxies, all but one of which have black hole masses $<10^9 M_\odot$, versus the 20 galaxies used in our fit, with 14 having $M_{BH} > 10^9 M_\odot$.

The measured rms scatter is almost identical for the r_b–σ_e and r_b–M_{BH} fits (0.24 dex versus 0.23 dex). The tightest relationship turns out to be between r_b and M_V, where the rms is 0.20 dex. The correlation coefficients indicate that all three relations are strong and statistically significant, with the strongest being that between r_b and M_{BH} ($r_s = 0.77$, $P = 7.3 \times 10^{-5}$). Both Lauer et al. (2007) and Dullo & Graham (2012) use a larger number of data points than ours in examining the r_b–σ_e and r_b–M_V relationships, and they find opposing results as to which parameter (σ_e or M_V) is better correlated with r_b; our results suggest that M_V is a better predictor of r_b than σ_e. (Note that the r_b–M_V correlation uses the *total* galaxy luminosity; if for the multi-component galaxies we use the luminosity of just the core-Sérsic component instead, the correlation is

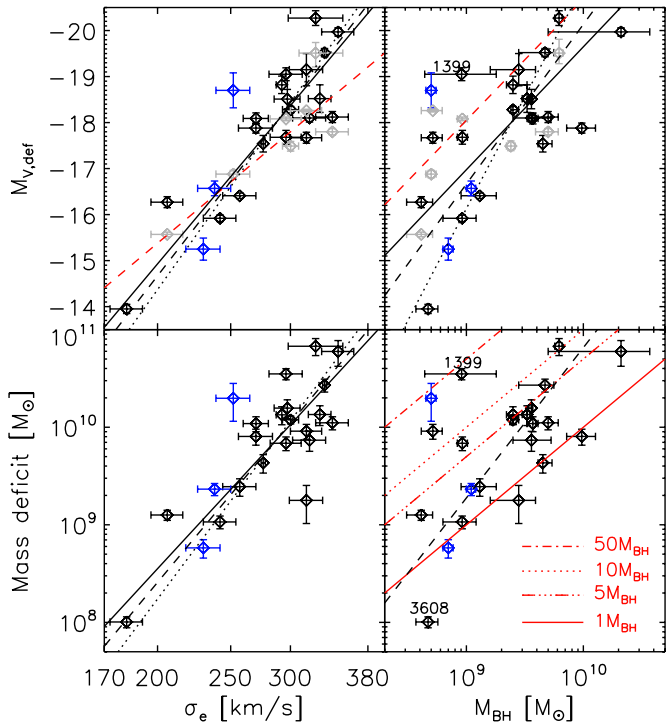

Figure 8. Upper panels: the plot of $M_{V,\rm def}$ vs. σ_e and $M_{\rm BH}$. $M_{V,\rm def}$ is the magnitude of the light deficit in the center, measured in the V band. The black diamonds show light deficit measurements for all 20 galaxies; the additional three galaxies (NGC 4552, NGC 5813, and NGC 5846) are shown in blue. The gray points, for the seven galaxies we have in common with KB09, mark the light deficit values from that paper. The dashed red lines are the relation reported in KB09. The black lines are our fits to the black diamonds: solid lines for direct fits (x-axis variables as predictors), dotted for reverse fits, and dashed lines for bisector fits; see Table 6. Lower panels: mass deficits $M_{\star,\rm def}$ plotted against the velocity dispersions (left) and black hole masses (right). The symbols here are the same as in the upper panels.

(A color version of this figure is available in the online journal.)

weaker and only marginally significant, with $r_s = -0.41$ and $P = 0.070$.) Despite the moderately large scatter, the r_b–$M_{\rm BH}$ relation is apparently the strongest one among the three, suggesting that $M_{\rm BH}$ is the most relevant parameter for determining r_b.

Figure 8 explores relationships between the light or mass deficit in the core and the black hole mass or the stellar velocity dispersion. The upper left panel shows the plot of the light deficit in the V band versus the stellar velocity dispersion calculated within the effective radius σ_e. The correlation between stellar velocity dispersion of host galaxies and $M_{V,\rm def}$ determined in KB09 is overplotted in red. Note that the velocity dispersion used to construct the latter correlation is defined differently: it is based on the velocity dispersion averaged within a slit aperture with a length of two half-light radii. Although there is probably no significant difference between these two methods of determining σ_e, this means that the individual data points cannot be strictly compared to the KB09 relation. For seven galaxies that overlap with KB09's sample, we indicate their values of light deficit using gray diamonds. On average, our values are more negative (i.e., more luminous) than those of KB09 by 0.30 mag, and the rms of the difference is 1.15 mag. In the upper right panel of Figure 8, the plot between $M_{V,\rm def}$ and the black hole masses is shown. Similarly, we overplot the correlation between these two quantities, as derived in KB09, in red.

Coefficients of the fits plotted in Figure 8 are listed in Table 6. The meaning of the coefficients is the same as in Equation (12), except now y corresponds to either $M_{V,\rm def}$ or $\log M_{\star,\rm def}$. In the direct fits, the independent variables are either $\log \sigma_e$ or $\log M_{\rm BH}$.

Compared to KB09, our $M_{V,\rm def}$–σ_e correlation is steeper and our $M_{V,\rm def}$–$M_{\rm BH}$ exhibits a shift toward a larger $M_{\rm BH}$ at a given value of light deficit. This highlights the difference between estimates based on the $M_{\rm BH}$–σ relation and the more reliable dynamical estimates of $M_{\rm BH}$ that we use. The scatter is notably higher in the $M_{V,\rm def}$–$M_{\rm BH}$ diagram, opposite to what is found in KB09.

The most interesting relation from a theoretical point of view is that between the *mass* deficit and the black hole mass, since this is the quantity that simulations predict (see references in the Introduction). The lower panels of Figure 8 show this relation, and also the relation between mass deficit and velocity dispersion; the coefficients of the fits are in the bottom half of Table 6. The large intrinsic scatter (and the large rms values) that we derive indicate that the linear fit is not representing the data well.

Of the seven correlations we have examined (Figures 7 and 8), those between r_b and $M_{\rm BH}$ and between $M_{V,\rm def}$ and σ_e appear to be the strongest ($r_s = 0.77$ and -0.75, respectively). Moreover, the rms scatter in $\log M_{\rm BH}$ for the fit between $M_{\rm BH}$ and r_b is only 0.30 dex (it is 0.35 dex for the correlation with $M_{\star,\rm def}$ and 0.33 dex for that with the light deficit). This is comparable to or even lower than the typical rms scatter for the $M_{\rm BH}$–σ relation (e.g., Park et al. 2012; Graham & Scott 2013; McConnell & Ma 2013). This suggests that measuring r_b can allow one to estimate $M_{\rm BH}$ (in core galaxies) with a precision similar to that obtained using the $M_{\rm BH}$–σ relation, without the need for spectroscopy. We give here the corresponding equation (derived from the fits in Table 5):

$$\log\left(\frac{M_{\rm BH}}{3\times10^9 M_\odot}\right) = (0.59\pm0.16) + (0.92\pm0.20)\log\left(\frac{r_b}{\rm kpc}\right);$$
$$\epsilon = 0.28\pm0.06 \text{ dex}. \quad (13)$$

The ratio between $M_{\star,\rm def}$ and $M_{\rm BH}$ seems to vary strongly, but is biased toward the low end of the range. Most galaxies have a mass deficit between 1 and 5 $M_{\rm BH}$, and the median value is 2.2 $M_{\rm BH}$. In three galaxies (IC 1459, NGC 3842, and NGC 5813), the mass deficit is just below the black hole mass. NGC 3608 has a remarkably low mass deficit of only 0.21 $M_{\rm BH}$. The largest mass deficit that we find is just below 40 $M_{\rm BH}$, occurring in NGC 1399. This unusually large value should perhaps be taken with a grain of salt, however, given the large uncertainty in the black hole mass of NGC 1399. The two publications that have presented dynamical measurements of the black hole mass (Houghton et al. 2006; Gebhardt et al. 2007) provide values that differ by almost a factor of three, and neither measurement included the dark matter halo in the modeling, which could likely result in underestimating $M_{\rm BH}$ and thereby overestimating the ratio between the mass deficit and $M_{\rm BH}$ (see Paper I). The next-largest mass deficit is 18 times $M_{\rm BH}$ in NGC 4261, with the one other galaxy having a mass deficit larger than $10M_{\rm BH}$ being NGC 4486. The broad range of $M_{\star,\rm def}/M_{\rm BH}$ (between 0.2 and 18 if we exclude NGC 1399) is in better agreement with Dullo & Graham (2012) than with KFCB09. The former also shows a number of galaxies having mass deficits of 1–4 $M_{\rm BH}$ while the latter has no galaxies in their sample with mass deficits below 5 $M_{\rm BH}$. Considering that KFCB09 and Kormendy & Bender (2009) use mostly outdated $M_{\rm BH}$ values and an old $M_{\rm BH}$–σ

Table 6
Relations between Light/Mass Deficits and Galaxy Parameters

Fit Type	a	b	ϵ	rms	r_s	P
	$M_{V,\rm def}$ vs. $(\sigma_e/200\ {\rm km\ s^{-1}})$				−0.75	0.00013
Direct	-14.93 ± 0.48	-19.53 ± 2.82	0.68 ± 0.18	0.70		
Reverse	-14.37 ± 0.54	-23.09 ± 3.10	0.70 ± 0.21	0.78		
Bisector	-14.67 ± 0.36	-21.16 ± 2.11	0.69 ± 0.20	0.73		
	$M_{V,\rm def}$ vs. $(M_{\rm BH}/3 \times 10^9 M_\odot)$				−0.59	0.0059
Direct	-18.25 ± 0.28	-2.67 ± 0.73	1.14 ± 0.24	1.07		
Reverse	-18.45 ± 0.41	-4.86 ± 1.32	1.53 ± 0.56	1.57		
Bisector	-18.32 ± 0.23	-3.47 ± 0.71	1.34 ± 0.43	1.20		
	$(M_{\star,\rm def}/3 \times 10^9 M_\odot)$ vs. $(\sigma_e/200\ {\rm km\ s^{-1}})$				0.68	0.00098
Direct	8.55 ± 0.23	8.38 ± 1.35	0.34 ± 0.09	0.36		
Reverse	8.24 ± 0.27	10.36 ± 1.62	0.35 ± 0.12	0.41		
Bisector	8.41 ± 0.17	9.27 ± 1.10	0.34 ± 0.11	0.38		
	$(M_{\star,\rm def}/3 \times 10^9 M_\odot)$ vs. $(M_{\rm BH}/3 \times 10^9 M_\odot)$				0.57	0.0086
Direct	9.97 ± 0.13	1.10 ± 0.34	0.54 ± 0.11	0.51		
Reverse	10.09 ± 0.21	2.27 ± 0.74	0.76 ± 0.32	0.79		
Bisector	10.01 ± 0.12	1.54 ± 0.33	0.65 ± 0.24	0.58		

Notes. As for Table 5, but now showing coefficients of fits (and overall correlations) between light deficit $M_{V,\rm def}$ or mass deficit $M_{\star,\rm def}$ of the core and either σ_e or $M_{\rm BH}$ of the galaxy. The rms residuals are for $M_{V,\rm def}$ in the first two relations and for log $M_{\star,\rm def}$ in the second two.

relationship for their analysis, it is likely that their ratios of $M_{\star,\rm def}/M_{\rm BH}$ are simply too high. (For the seven of our galaxies in common with those in Kormendy & Bender 2009, we find that their mass deficits are somewhat higher than ours—median ratio ∼1.2—while their black hole masses are only ∼55% of ours.) The simulations of Gualandris & Merritt (2008) indicate that mass deficits up to 5 $M_{\rm BH}$ can be generated from single dry mergers. Therefore, our results can probably be explained with a reasonably low number of major dry mergers. Low $M_{\star,\rm def}/M_{\rm BH}$ ratios could also be obtained if gas to refill the core via new star formation is available (i.e., the merger is "wet").

Why does r_b correlate so well with $M_{\rm BH}$, while the light and the mass deficit do not? We note that our estimate of $M_{\rm V,def}$, from which the mass deficit is in turn derived, is based on the assumption that the inward extrapolation of the outer Sérsic fit is the correct representation of the inner projected density profile of the galaxy before the binary black hole scouring takes place. This might not be the case for real galaxies, and the large scatter about the relations of Figure 8 could simply reflect this (see, e.g., Hopkins & Hernquist 2010). The size of the core may be a more robust quantity in this respect. It will be interesting to investigate whether the internal kinematics of the galaxies change at this radius.

8. SUMMARY

We have presented measurements for cores in 23 elliptical galaxies, where the cores are clearly detected based on the criteria suggested in Trujillo et al. (2004). These detections and measurements were made using core-Sérsic fits to extended surface brightness profiles, the majority of which go out significantly beyond the half-light radius; for a quarter of the sample, we found that the best fits were with the sum of core-Sérsic and an outer envelope, the latter represented by an exponential or Sérsic component. For 20 of these galaxies, reliable $M_{\rm BH}$ measurements are available from the literature or from our own work (Paper I); the majority of these are derived from recent stellar dynamical modeling. We computed the light deficit in the core (assumed to be the result of supermassive black hole mergers which follow galaxy mergers) assuming that the original profile, before the core was formed, followed a Sérsic model matching the outer part of the galaxy, based on the core-Sérsic fit (or the outer part of the core-Sérsic component in the case of multi-component fits). We then derived the corresponding stellar mass deficit using stellar mass-to-light ratios from dynamical models, available for all of the galaxies in the sample.

We find that the size of the core (break radius r_b) is most strongly correlated with the black hole mass, while the second strongest correlation (and the linear fit with the lowest scatter) is with the luminosity of the host galaxy; the weakest correlation is that between the break radius and the galaxy's stellar velocity dispersion. The low scatter of the r_b–$M_{\rm BH}$ relation (0.30 dex when r_b is the independent variable) opens up the possibility of accurately estimating black hole masses in core galaxies without the need for spectroscopy.

The stellar mass deficits we derive range between 0.2 and 39 times the black hole mass; for about 75% of the sample, the range is 1–5 $M_{\rm BH}$, and the median value for the whole sample is 2.2 $M_{\rm BH}$. Given the results of recent simulations, these values can be explained by a reasonably small number of (dry) mergers.

We thank the anonymous referee for a number of useful comments that helped us significantly improve the paper.

S.P.R. was supported by the DFG Cluster of Excellence "Origin and Structure of the Universe." P.E. was supported by the Deutsche Forschungsgemeinschaft through the Priority Programme 1177 "Galaxy Evolution."

Some of the data presented in this paper were obtained using SINFONI at the Very Large Telescope (VLT) and from the Mikulski Archive for Space Telescopes (MAST). The VLT is operated by the European Southern Observatory on Cerro Paranal in the Atacama Desert of northern Chile. STScI is operated by the Association of Universities for Research in Astronomy, Inc., under NASA contract NAS5-26555.

This research is based in part on data from the Isaac Newton Group Archive, which is maintained as part of the CASU Astronomical Data Centre at the Institute of Astronomy, Cambridge.

Funding for the creation and distribution of the SDSS Archive has been provided by the Alfred P. Sloan Foundation, the Participating Institutions, the National Aeronautics and Space Administration, the National Science Foundation, the U.S. Department of Energy, the Japanese Monbukagakusho, and the Max Planck Society. The SDSS Web site is http://www.sdss.org/.

The SDSS is managed by the Astrophysical Research Consortium (ARC) for the Participating Institutions. The Participating Institutions are The University of Chicago, Fermilab, the Institute for Advanced Study, the Japan Participation Group, The Johns Hopkins University, the Korean Scientist Group, Los Alamos National Laboratory, the Max-Planck-Institute for Astronomy (MPIA), the Max-Planck-Institute for Astrophysics (MPA), New Mexico State University, University of Pittsburgh, University of Portsmouth, Princeton University, the United States Naval Observatory, and the University of Washington.

Finally, this work has made use of the NASA/IPAC Extragalactic Database (NED) which is operated by the Jet Propulsion Laboratory, California Institute of Technology, under contract with the National Aeronautics and Space Administration.

APPENDIX A

PHOTOMETRY OF IC 1459

We constructed the circularized *V*-band photometry of IC 1459 by matching *HST* and ground-based data. Inside 12″ we used an *HST* WFPC2 F814W profile (Proposal ID: 5454, PI: Marijn Franx) derived using the software of Bender & Moellenhoff (1987) while masking the central dusty features. At larger radii we used CCD data from Bender et al. (1989; see also Scorza et al. 1998), calibrated with photoelectric photometry available in Hyperleda.

APPENDIX B

PHOTOMETRY OF NGC 1399

The circularized *B*-band photometry of NGC 1399 was constructed by matching the extended profile considered in Saglia et al. (2000) to the profile derived using the IRAF software from an *HST* ACS F606W image (Proposal ID: 10129, PI: Thomas Puzia) of the galaxy in the inner 12″.

APPENDIX C

PHOTOMETRY OF NGC 1407

The light profile for this galaxy is based on that used in Paper I for the BH mass measurement. To facilitate the exploration of possible outer-envelope models (Section 4), we replaced the inner 7.″5 of the previous profile with data from a deconvolved version of the *HST*-ACS F435W image (20 iterations of Lucy–Richardson deconvolution). This allowed us to fit the profile without PSF convolution.

APPENDIX D

PHOTOMETRY OF NGC 3379

The light profile was constructed using WFPC2 F814W images from the *HST* archive (Proposal ID: 5512, PI: Sandra Faber) and SDSS *i*-band images. The PC chip image of *HST* was deconvolved using 20 rounds of Lucy–Richardson deconvolution and then the profile was measured through ellipse fitting. That profile was used for $r < 10''$. At larger radii, we used an ellipse-fit profile measured using a mosaic of SDSS *i*-band images, constructed using SWarp (Bertin et al. 2002). The SDSS *i*-band magnitudes were converted to Cousins *I* using an $r - i$ color of 0.44 (measured from ellipse fits to single SDSS *r* and *i* images) and the transformation of Jordi et al. (2006).

APPENDIX E

PHOTOMETRY OF NGC 3608

The surface brightness profile for NGC 3608 is a combination of ellipse fits to an F555W WFPC2 image (Proposal ID: 5454, PI: Marijn Franx) for $r_{eq} < 7''$ and ellipse fits to an SDSS *g*-band image for $r_{eq} > 7''$. The SDSS image was calibrated to *V*-band using the SDSS *g*- and *r*-band images and the color transformations of Lupton.[7] We matched the two data sets using fixed-ellipse-fit profiles to the SDSS image and the WFPC2 mosaic, using the overlap between 6–85″ to determine the best scaling and background subtraction to apply to the WFPC2 data.

APPENDIX F

PHOTOMETRY OF NGC 3842

The surface brightness profile for NGC 3842 is calibrated to the *V*-band and is assembled from three pieces. The innermost part ($a < 1.''2$) comes from the published F555 WFPC2 PC1 profile of L05. The profile in the intermediate radii is derived from an ellipse fit to an F555W WFPC2 mosaic image (galaxy center on WF3 chip; Proposal ID: 265, PI: Douglas Geiser). This is matched to an ellipse fit to an SDSS *g*-band image, including determining the level of sky background of the WFPC2 image. The combination then consists of WFPC2 data at $1.2 < a < 38''$ and SDSS data at $a > 38''$. The final surface brightness profile is constructed by matching the combined profile and the L05 profile.

APPENDIX G

PHOTOMETRY OF NGC 4291

For NGC 4291, the profile is a combination of ellipse fits to a WFPC2 F702W image (Proposal ID: 6357, PI: Walter Jaffe; see Rest et al. 2001) and ellipse fits to a Sloan *r*-band Isaac Newton Telescope Wide Field Camera (INT-WFC) image retrieved from the Isaac Newton Group (ING) Archive. The latter was a 120 s exposure originally obtained on 2004 January 24. The INT-WFC image was calibrated to the *V* band using aperture photometry from Prugniel & Heraudeau (1998). We matched the two data sets using fixed-ellipse-fit profiles to the INT-WFC image and the WFPC2 mosaic, using the overlap between 10–80″ to determine the best scaling and background subtraction to apply to the WFPC2 data. The final profile used data from the WFPC2 PC chip for $r < 7''$ and data from the INT-WFC image for $r > 7''$.

APPENDIX H

PHOTOMETRY OF NGC 5516

The profile for this galaxy was constructed by combining data from WFPC2 F814W images from the *HST* archive (Proposal ID: 6579, PI: John Tonry) and an *R*-band image from the Wide Field Imager of the ESO-MPI 2.2 m telescope. The sky background for the WFPC2 data was determined by matching

[7] http://www.sdss.org/dr7/algorithms/sdssUBVRITransform.html#Lupton2005

ellipse-fit profiles of the full WFPC2 mosaic with a profile from the WFI image. The PC chip image of *HST* was deconvolved using 20 rounds of Lucy–Richardson deconvolution and then the profile was measured through ellipse fitting; the resulting profile was used for $r < 9''$. At larger radii, we used an ellipse-fit profile from the WFI image.

APPENDIX I

PHOTOMETRY OF NGC 5813

The profile for this galaxy is a combination of ellipse fits to an F814W WFPC2 image (Proposal ID: 5454, PI: Marijn Franx) and an SDSS *i*-band image. Since patchy dust was present in the nucleus, we combined the F814W image with the corresponding F555W image to perform a simple dust extinction correction on the F814W image. Sky backgrounds for the two filters were determined by matching ellipse-fit profiles of the full WFCP2 mosaic image with ellipse-fit profiles from the sky-subtracted SDSS *g* and *i* images. The F555W and F814W images were also used, along with the prescriptions in Holtzman et al. (1995), to generate *V*-band and *I*-band calibrations for each, iterating from an initial guess for the central ($r < 10''$) $V - I$ color until the measured color converged. We then formed a $V - I$ PC-chip image and used this to color-correct the F814W PC image, assuming a simple screen model for the dust. The final profile used the (extinction-corrected) WFPC2 PC-chip data for $r < 2\farcs8$ and SDSS *i*-band data at larger radii.

APPENDIX J

PHOTOMETRY OF NGC 5846

Since NGC 5846 had available the same kind of data as NGC 5813 *and* similar patchy dust extinction in the circumnuclear region, we followed an essentially identical process for this galaxy. The final profile used the (extinction-corrected) WFPC2 PC-chip data for $r < 15''$ (Proposal ID: 5920, PI: Jean Brodie) and SDSS *i*-band data at larger radii (the difference in transition radius compared with NGC 5813 is due to the larger extent of circumnuclear dust in NGC 5846).

APPENDIX K

PHOTOMETRY OF NGC 6086

We used a WFPC2 F814W image (proposal ID: 7281, PI: Roberto Fanti) and an SDSS *i*-band image to construct the surface brightness profile based on combined ellipse fits. The part of the profile inside $11''$ comes from the PC chip of WFPC2, and the innermost $1\farcs5$ is from the PC chip of WFPC2 after performing 20 rounds of Lucy–Richardson deconvolution. The light profile is calibrated to the *R* band. This was done by first converting the SDSS *i*-band profile to SDSS *r* by matching with a profile from the SDSS *r*-band image. The SDSS *r*-band magnitudes were then converted to Cousins *R* using a $g - r$ color of 0.95 (measured from the SDSS *g* and *r* images) and the conversion of Jordi et al. (2006).

APPENDIX L

PHOTOMETRY OF NGC 7768

The light profile of NGC 7768 is mostly based on WFPC2 F814W images (Proposal ID: 8184, PI: P. Côté), which were combined to make both a PC image and a mosaic. The PC image was corrected for dust extinction using the F814W image and F450W WFPC2 images, but there was still considerable residual extinction inside $1''$, so an *HST*-NICMOS2 F160W image was used for the inner region. The final profile is obtained through ellipse fits to the following: (1) NICMOS F160W image for $a < 0\farcs93$, (2) WFPC2 F814W PC image for *a* between 0.93 and $10''$, and (3) WFPC2 F814W mosaic for $a > 10''$.

The F814W image was corrected for sky background by matching a fixed-ellipse-fit profile with a similar fixed-ellipse-fit profile from an *r*-band image with the Isaac Newton Telescope Wide Field Camera (100 s, 2002 December 3), taken from the Isaac Newton Group archive. The profiles were calibrated to the *V* band using aperture photometry from Prugniel & Heraudeau (1998; specifically, the INT-WFC *r*-band image was calibrated to *V*, and then the WFPC2 F814W profile was matched to the INT-WFC *r*-band profile.)

APPENDIX M

COMPARISON WITH THE SÉRSIC FITTING OF KFCB09

Of all the galaxies presented in Figure 7, there are five galaxies which are also part of KB09 sample, i.e., NGC 4472, NGC 4486 (M87), NGC 4649, NGC 4261, and NGC 4374. Using the photometric data available in KFCB09, we derive the missing light using the core-Sérsic function as described in Sections 2 and 6. From these five measurements, we find that some of our $M_{V,\mathrm{def}}$ fall outside the uncertainties provided by KB09. The difference is largest for NGC 4486 and NGC 4261 (by $\sim$0.7 mag or a factor of two in luminosity) and it is not systematic. The disagreement probably reflects the different details that were involved in the fitting and the derivation of the missing light.

1. We use the circularized radius; KFCB09 uses the semimajor axis radius. Galaxies are not perfectly round or circular in projection. Non-zero ellipticity anywhere in the galaxy, not just in the center, will induce a deviation in $M_{V,\mathrm{def}}$ since the light deficit in both KFCB09 and this work depends also on the Sérsic fit to the outer part of the galaxy. The magnitude of the deviation is difficult to estimate, since this depends very much on the characteristics of each galaxy.
2. A different fitting range introduces more discrepancies. Because we use circularized radius, we can use only the data points for which the ellipticity is given. In the photometric profiles of KFCB09, the ellipticity is often not specified for a few innermost or outermost radii; therefore, we cannot use those points in our fits. In addition, in the particular case of NGC 4486, KB09 used a Sérsic fit (from KFCB09, using the semimajor axis) that excluded data outside $400''$, because it apparently gave rise to a Sérsic index that was too large (almost 12) due to the cD halo. However, we found no difficulties in fitting a core-Sérsic function to the entire profile (out to $\sim 1000''$), using the circularized radius; we obtain a Sérsic index of 8.9 (almost identical to KFCB09's value), albeit with different values of r_e and μ_e.
3. We fit the galaxy profile with a core-Sérsic profile, and KFCB09 fit the outer part of the galaxy with a Sérsic profile. The critical point is the transition region between the Sérsic and the core. In the way KFCB09 defines the core, there is no transition region: the core immediately starts when the Sérsic model no longer fits the data points in the inner part. We use a core-Sérsic parameterization and since we fit the α parameter, instead of fixing it to infinity, we allow some part of the galaxy to be partly Sérsic, partly power-law. This leads to a different inner limit of the radial range that

is fitted only by the Sérsic model, which in the end results in a different best-fitting Sérsic profile.

4. The light deficit in KB09 is obtained by calculating the difference of the integrated intensity between the extrapolated Sérsic function and the actual (observed) profile after PSF deconvolution. The ellipticity of the Sérsic model is fixed to the ellipticity at the inner limit of the fitted radial range. Since some of our light profiles are not PSF-deconvolved, we instead compute the difference between the best-fitting core-Sérsic function and the extrapolated Sérsic component. We also implicitly assume an ellipticity of zero when integrating the extrapolated Sérsic function, since we have used a circularized profile in the first place.

REFERENCES

Begelman, M. C., Blandford, R. D., & Rees, M. J. 1980, Natur, 287, 307
Bender, R., Capaccioli, M., Macchetto, F., & Nieto, J. L. 1989, Msngr, 55, 6
Bender, R., & Moellenhoff, C. 1987, A&A, 177, 71
Bertin, E., Mellier, Y., Radovich, M., et al. 2002, in ASP Conf. Ser. 281, Astronomical Data Analysis Software and Systems XI, ed. D. A. Bohlender, D. Durand, & T. H. Handley (San Francisco, CA: ASP), 228
Byun, Y.-I., Grillmair, C. J., Faber,, et al. 1996, AJ, 111, 1889
Caon, N., Capaccioli, M., & D'Onofrio, J. 1993, MNRAS, 265, 1013
Cappellari, M., Bacon, R., Bureau, M., et al. 2006, MNRAS, 366, 1126
Cappellari, M., Bacon, R., Davies, R. L., et al. 2008, in IAU Symp. 245, Formation and Evolution of Galaxy Bulges, ed. M. Bureau, E. Athanassoula, & B. Barbuy (Cambridge: Cambridge Univ. Press), 215
Cappellari, M., McDermid, R. M., Alatalo, K., et al. 2012, Natur, 484, 485
Cappellari, M., McDermid, R. M., Alatalo, K., et al. 2013, MNRAS, 432, 1862
Cappellari, M., Verolme, E. K., van der Marel, R. P., et al. 2002, ApJ, 578, 787
Ciotti, L., & Bertin, G. 1999, A&A, 352, 447
Conroy, C., & van Dokkum, P. G. 2012, ApJ, 760, 71
de Vaucouleurs, G. 1948, AnAp, 11, 247
de Vaucouleurs, G., de Vaucouleurs, A., Corwin, H. G., Jr., et al. 1991, Third Reference Catalogue of Bright Galaxies (Berlin: Springer-Verlag)
Donzelli, C. J., Muriel, H., & Madrid, J. P. 2011, ApJS, 195, 15
Dullo, B. T., & Graham, A. W. 2012, ApJ, 755, 163
Dullo, B. T., & Graham, A. W. 2013, ApJ, 768, 36
Ebisuzaki, T., Makino, J., & Okumura, S. K. 1991, Natur, 354, 212
Faber, S. M., Tremaine, S., Ajhar, E. A., et al. 1997, AJ, 114, 1771
Ferrarese, L., Côté, P., Jordán, A., et al. 2006, ApJS, 164, 334
Ferrarese, L., Ford, H. C., & Jaffe, W. 1996, ApJ, 470, 444
Ferrarese, L., van den Bosch, F. C., Ford, H. C., et al. 1994, AJ, 108, 1598
Gebhardt, K., Lauer, T. R., Pinkney, J., et al. 2007, ApJ, 671, 1321
Gebhardt, K., & Thomas, J. 2009, ApJ, 700, 1690
Gonzalez, A. H., Zabludoff, A. I., & Zaritsky, D. 2003, Ap&SS, 285, 67
Gonzalez, A. H., Zabludoff, A. I., & Zaritsky, D. 2005, ApJ, 618, 195
Graham, A. W. 2004, ApJL, 613, L33
Graham, A. W., & Driver, S. P. 2005, PASA, 22, 118
Graham, A. W., Erwin, P., Trujillo, I., & Asensio Ramos, A. 2003, AJ, 125, 2951
Graham, A. W., Onken, C. A., Athanassoula, E., et al. 2011, MNRAS, 412, 2211
Graham, A. W., & Scott, N. 2013, ApJ, 764, 151
Gualandris, A., & Merritt, D. 2008, ApJ, 678, 780
Gültekin, K., Richstone, D. O., Gebhardt, K., et al. 2009, ApJ, 698, 198
Häring, N., & Rix, H. 2004, ApJL, 604, L89
Holtzman, J. A., Burrows, C. J., Casertano, S., et al. 1995, PASP, 107, 1065
Hopkins, P. F., & Hernquist, L. 2010, MNRAS, 407, 447
Hopkins, P. F., Lauer, T. R., Cox, T. J., Hernquist, L., & Kormendy, J. 2009, ApJS, 181, 486
Houghton, R. C. W., Magorrian, J., Sarzi, M., et al. 2006, MNRAS, 367, 2
Hu, J. 2008, MNRAS, 386, 2242
Huang, S., Ho, L. C., Peng, C. Y., Li, Z. Y., & Barth, A. J. 2013, ApJ, 766, 47
Jordi, K., Grebel, E. K., & Ammon, K. 2006, A&A, 460, 339
Kelly, B. C. 2007, ApJ, 665, 1489
Kormendy, J., & Bender, R. 2009, ApJL, 691, L142
Kormendy, J., Dressler, A., Byun, Y. I., et al. 1994, in ESO/OHP Workshop on Dwarf Galaxies, ESO Conference and Workshop Proceedings, ed. G. Meylan & P. Prugniel (Garching: ESO), 147
Kormendy, J., Fisher, D. B., Cornell, M. E., & Bender, R. 2009, ApJS, 182, 216
Kormendy, J., & Ho, L. 2013, ARA&A, 51, 511
Kormendy, J., & Richstone, D. 1995, ARA&A, 33, 581
Kronawitter, A., Saglia, R. P., Gerhard, O., & Bender, R. 2000, A&AS, 144, 53
Lauer, T. R. 2012, ApJ, 759, 64
Lauer, T. R., Ajhar, E. A., Byun, Y.-I., et al. 1995, AJ, 110, 2622
Lauer, T. R., Faber, S. M., Gebhardt, K., et al. 2005, AJ, 129, 2138
Lauer, T. R., Faber, S. M., Richstone, D., et al. 2007, ApJ, 662, 808
Laurikainen, E., Salo, H., Buta, R., Knapen, J. H., & Comerón, S. 2010, MNRAS, 405, 1089
Levenberg, K. 1944, QApMa, 2, 164
Magorrian, J., Tremaine, S., Richstone, D., et al. 1998, AJ, 115, 2285
Makino, J., & Ebisuzaki, T. 1996, ApJ, 465, 527
Marquardt, D. 1963, J. SIAM, 11, 431
McConnell, N. J., & Ma, C.-P. 2013, ApJ, 764, 184
McConnell, N. J., Ma, C.-P., Gebhardt, K., et al. 2011a, Natur, 480, 215
McConnell, N. J., Ma, C.-P., Graham, J. R., et al. 2011b, ApJ, 728, 100
McConnell, N. J., Ma, C.-P., Murphy, J. D., et al. 2012, ApJ, 756, 179
Merritt, D. 2006, ApJ, 648, 976
Milosavljević, M., & Merritt, D. 2001, ApJ, 563, 34
Nakano, T., & Makino, J. 1999, ApJ, 510, 155
Park, D., Kelly, D. C., Woo, J.-H., & Treu, T. 2012, ApJS, 203, 6
Prugniel, P., & Heraudeau, P. 1998, A&AS, 128, 299
Pu, S. B., Saglia, R. P., Fabricius, M. H., et al. 2010, A&A, 516, A4
Rest, A., van den Bosch, F. C., Jaffe, W., et al. 2001, AJ, 121, 2431
Richings, A. J., Uttley, P., & Körding, E. 2011, MNRAS, 415, 2158
Richstone, D., Ajhar, E. A., Bender, R., et al. 1998, Natur, 395, A14
Rusli, S., Thomas, J., Saglia, R. P., et al. 2013, AJ, 146, 45
Saglia, R. P., Bertschinger, E., Baggley, G., et al. 1993, MNRAS, 264, 961
Saglia, R. P., Kronawitter, A., Gerhard, O., & Bender, R. 2000, AJ, 119, 153
Schlegel, D. J., Finkbeiner, D. P., & Davis, M. 1998, ApJ, 500, 525
Schulze, A., & Gebhardt, K. 2011, ApJ, 729, 21
Scorza, C., Bender, R., Winkelmann, C., Capaccioli, M., & Macchetto, D. F. 1998, A&AS, 131, 265
Seigar, M. S., Graham, A. W., & Jerjen, H. 2007, MNRAS, 378, 1575
Sérsic, J. L. 1963, BAAA, 6, 41
Sérsic, J. L. 1968, Atlas de Galaxias Australes (Cordoba: Observatorio Astronomico)
Shen, J., & Gebhardt, K. 2010, ApJ, 711, 484
Shields, G. A., Menezes, K. L., Massart, C. A., & Vanden Bout, P. 2006, ApJ, 641, 683
Smith, R. J., & Lucey, J. R. 2013, MNRAS, 434, 1964
Turner, M. L., Côté, P., Ferrarese, L., et al. 2012, ApJS, 203, 5
Thomas, J., Saglia, R. P., Bender, R., et al. 2007, MNRAS, 382, 657
Thomas, J., Saglia, R. P., Bender, R., et al. 2011, MNRAS, 415, 545
Tremaine, S., Gebhardt, K., Bender, R., et al. 2002, ApJ, 574, 740
Trujillo, I., Erwin, P., Asensio Ramos, A., & Graham, A. W. 2004, AJ, 127, 1917
van den Bosch, R. C. E., & de Zeeuw, P. T. 2010, MNRAS, 401, 1770
van den Bosch, R. C. E., Gebhardt, K., Gültekin, K., et al. 2012, Natur, 491, 729
Walsh, J. L., Barth, A. J., & Sarzi, M. 2010, ApJ, 721, 762
Wegner, G. A., Corsini, E. M., Thomas, J., et al. 2012, AJ, 144, 78